2010

Image Processing Algorithms for Diagnostic Analysis of Microcirculation

Sumeyra Ummuhan Demir
Virginia Commonwealth University

Virginia Commonwealth University
Department of Electrical and Computer Engineering

This is to certify that the dissertation prepared by Sümeyra Ü Demir entitled IMAGE PROCESSING ALGORITHMS FOR DIAGNOSTIC ANALYSIS OF MICROCIRCULATION has been approved by her committee as satisfactory completion of the Thesis Dissertation requirement for the degree of Doctor of Philosophy.

Rosalyn S. Hobson, PhD, Advisor, Department of Electrical and Computer Engineering

---

Kayvan Najarian, PhD, Co-Advisor, Computer Science Department

---

Kevin R. Ward, MD, Emergency Medicine Department

Alen Docef, PhD, Department of Electrical and Computer Engineering

---

Afroditi V. Filippas, PhD, Department of Electrical and Computer Engineering

Date:

IMAGE PROCESSING ALGORITHMS FOR DIAGNOSTIC ANALYSIS OF MICROCIRCULATION

A dissertation submitted in partial fulfillment of the requirements for the degree of Doctor of Philosophy at Virginia Commonwealth University.

by

SÜMEYRA Ü DEMIR

Advisor: ROSALYN S. HOBSON

Associate Professor, Department of Electrical and Computer Engineering

Virginia Commonwealth University

Richmond, VA

August, 2010

ACKNOWLEDGMENT

This dissertation would not be possible without the continuous support of my family, friends and advisors. I would like to thank my parents who always believed in me, and my sister for being with me during the hard times. I would also like to thank my brothers for their love and support.

I am thankful to my co-advisor; Dr. Kayvan Najarian for walking with me on this journey, leading with his intelligence and knowledge, my advisor; Dr. Rosalyn Hobson for her continous support, my friends in the lab, my roommate and all other 'real' friends for making life easier.

Thanks.

Contents

List of Figures

List of Tables

ABSTRACT

IMAGE PROCESSING ALGORITHMS FOR DIAGNOSTIC ANALYSIS OF MICROCIRCULATION

by Sumeyra Ummuhan Demir, Ph.D

A Dissertation submitted in partial fulfillment of the requirements for the degree of Doctor of Philosophy at Virginia Commonwealth University.

Virginia Commonwealth University, 2010

Major Director: Rosalyn S. Hobson, Ph.D
Associate Professor, Virginia Commonwealth University

Microcirculation has become a key factor for the study and assessment of tissue perfusion and oxygenation. Detection and assessment of the microvasculature using videomicroscopy from the oral mucosa provides a metric on the density of blood vessels in each single frame. Information pertaining to the density of these microvessels within a field of view can be used to quantitatively monitor and assess the changes occurring in tissue oxygenation and perfusion over time. Automated analysis of this information can be used for real-time diagnostic and therapeutic planning of a number of clinical applications including resuscitation.

The objective of this study is to design an automated image processing system to segment microvessels, estimate the density of blood vessels in video recordings, and identify the distribution of blood flow. The proposed algorithm consists of two main stages: video processing and image segmentation. The first step of video processing is stabilization. In the video stabilization step, block matching is applied to the video frames. Similarity is measured by cross-correlation coefficients. The main technique used in the segmentation step is multi-thresholding and pixel verification based on calculated geometric and contrast parameters. Segmentation results and differences of video frames are then used to identify the capillaries with blood flow. After categorizing

blood vessels as active or passive, according to the amount of blood flow, quantitative measures identifying microcirculation are calculated.

The algorithm is applied to the videos obtained using Microscan Side-stream Dark Field (SDF) imaging technique captured from healthy and critically ill humans/animals. Segmentation results were compared and validated using a blind detailed inspection by experts who used a commercial semi-automated image analysis software program, AVA (Automated Vascular Analysis). The algorithm was found to extract approximately 97% of functionally active capillaries and blood vessels in every frame.

The aim of this study is to eliminate the human interaction, increase accuracy and reduce the computation time. The proposed method is an entirely automated process that can perform stabilization, pre-processing, segmentation, and microvessel identification without human intervention. The method may allow for assessment of microcirculatory abnormalities occurring in critically ill and injured patients including close to real-time determination of the adequacy of resuscitation.

Chapter 1

Novelty and Contributions

Flow in blood vessels smaller than 100 μm (defined as the microcirculation) plays a significant role in various vital functions in the human body [3]. Several rheological properties of blood in microcirculation, in particular viscosity make circulation of red blood cells and plasma in capillaries noticeable and different from that of large blood vessels [4] [5]. The capillary network is responsible for transporting nutrients, fluids and oxygen to all tissues [6, 7, 8, 9]. Global hemodynamic measurements derived from cardiac output, blood pressure and oxygen delivery are not sufficient to predict the level of microvascular oxygen delivery [10, 11]. Therefore, the knowledge of healthy distribution and circulation of blood in capillaries and small blood vessels has always been regarded as a key aspect of physiological health [3].

Study of microcirculation has revealed potential diagnostic value in illnesses and diseases such as sepsis [12], sickle cell [13, 14], chronic ulcers, diabetes mellitus and hypertension [15, 16]. In each of these diseases, several characteristics of microcirculation such as structure of capillaries and quality of blood flow in the capillaries change over time [17, 18, 19, 20, 21]. A technology that can quantitatively detect and screen microcirculatory changes can greatly assist in the early detection of these pathological conditions, and therefore provide improved opportunities for treatment [22]. Moreover such an automated technology can avoid over and under resuscitation by real-time analysis of microcirculation and as such greatly improve the outcome of resuscitation.

More than 1000 people die per day in the United States as a result of poor cardiac arrest and trauma resuscitation outcomes [23]. The Post-Resuscitative and Initial Utility in Life Saving Efforts (PULSE) workshop was organized to seek opportunities to improve outcomes following resuscitation

in 2000 [23, 24]. The workshop was sponsored by the National Heart Lung and Blood Institute of the National Institutes of Health, as well as other federal agencies including the Department of Defense. An expert panel recommended specific items to advance the technology of resuscitation research, which includes improving technology based methodologies for monitoring and performing resuscitation [25].

Stadlbauer et al. stated [26]: "In 1990, about 5 million people died worldwide as a result of injury, and it seems likely that the global epidemic of deadly trauma is only beginning. By 2020, deaths from injury are expected to increase to 8 million worldwide [27], and 30% of these fatalities will be attributable to hemorrhagic shock [28]. Resuscitation of patients in uncontrolled hemorrhagic shock remains one of the most challenging aspects of emergency care, and trauma patients with complete cardiovascular collapse have an extremely poor chance of survival."

Knowing that, a system that increases the chance of survival of trauma patients by closely monitoring microcirculation in real time would represent a significant improvement. Particularly in trauma care, it is highly desirable to monitor the changes of microcirculation during resuscitation and decide when to start and/or stop resuscitation according to real-time quantitative analysis of microcirculation [29, 30, 31]. Such an automated analysis will greatly help avoid over- and under-resuscitation.

Automated analysis of microcirculatory videos may also have a tremendous impact on hemorrhagic shock cases. Hemorrhagic shock is a leadingcause of death in trauma patients [32]. In addition, it is reported that 50% of deaths caused by serious injuries are preceded by circulatory system collapses [33]. While resuscitation is known to help many of such patients, under- and over-resuscitation are known to be the main factors for failure of this intervention. The main reason of the failure is that resuscitation is often conducted without monitoring the true factors reflecting blood circulation. As such, the proposed system that allows care providers to automatically monitor the changes in microcirculation during resuscitation can significantly impact the success of the resuscitation attempt. The proposed system helps decide when to start or stop resuscitation so as to avoid under- and over- resuscitation. The significance of this automated system is that; the close to real-time assessment of microcirculation can control the timing and planning of resuscitation, and therefore help save many lives.

The objective of this research is to design an automated system for quantitative analysis of microcirculation video recordings. A fully automated analysis of video microscopy of the circulation has potential clinical value in diagnosis and treatment of diseases. Detecting microcirculatory abnormalities occurring in critically ill and injured patients may also detect occult hypo-perfusion as well as help determine the adequacy of resuscitation. The system will utilize advanced image processing techniques to segment microcirculation videos and to estimate the features of blood flow. In cases of resuscitation application, the real-time feedback from the proposed system may have the capability to produce a warning system to prevent over- and under-resuscitation subjects.

The novelty of the algorithm developed for this proposal can be divided into three key components:

1. Digital image stabilization algorithms generate a compensated video sequence to deal with undesirable camera shake or subject movements. A novel automated method to stabilize video frames and label frames which are in transition is proposed. Block matching and maximizing correlation coefficients are utilized to stabilize video frames. Although block matching and correlation methods are relatively routine video stabilization techniques, in this application the proposed system ensures that the blocks to be matched include objects of interest - blood vessels. Ensuring the blocks do not consist of only background pixels improves the effectiveness and computational complexity of the stabilization process. Along with stabilization, the algorithm is also capable of identifying the frames where the scene changes. The details of this method are provided in Chapter 6, the Stabilization section.

2. A method based on multi-thresholding and pixel verification is proposed to segment blood vessels in microcirculation video recordings. The combination of multi-thresholding methodology, a technique for verification of vessel candidates when segmenting blood vessels, pre-processing steps, and the option to modify decision parameters forms a novel and effective segmentation approach. In the pre-processing step, changing parameters of histogram equalization according to the threshold level improves the use of multi-level thresholding. Due to the low quality of microcirculation images, without the pre-processing step thresholding at different levels performs poorly and inefficiently. Changing pre-processing parameters at each threshold level results in different size of blood vessels at different threshold levels. Chapter

5 provides a detailed description of the segmentation algorithm and the pre-processing step. The algorithm is capable of segmenting blood vessels from microcirculation videos as well as retinal images.

3. The method presented in this dissertation uses the original video frames and the segmentation results of the averaged frames to automatically detect blood vessels without flow. In existing practices, detecting blood vessels with flow and calculating quantitative measurements of microcirculation is a manual process. The presented algorithm is capable of identifying capillaries with blood flow automatically using pixel intensity differences. The novelty of this approach is the calculation of quantitative microcirculation parameters using a fully automated system. The details of the algorithm are presented in Chapter 4, under Difference Calculation section.

Chapter 2

Background

Although macrocirculation distributes the blood globally throughout the whole body, microcirculation is the primary site of oxygen, fluid and nutrient exchange between blood and tissue, hormone delivery from endocrine glands, bulk delivery between organs and waste product removal [3]. Researchers have been studying human microcirculation since the late nineteenth century [34]. Microscope combined with a magnifying lens was the very first tool to visually assess skin microcirculation [10, 34]. In 1879, Heuter investigated the capillary network on the inner border of human lip using a microscope [35]. Introduction of intra-vital microscopy into clinical studies led to further research on anatomy, physiology and pathology of human skin microcirculation. Müller presented his findings in two large volumes in 1937 and 1939 including a large collection of color capillaroscopic images, painted by himself [36] .

In 1922, decreasing capillary density (CD) was linked with sepsis by Freedlander and Lenhart [37]. Studies followed examining microvascular pathology in several conditions such as ischaemic limb, Raynaud's phenomenon and systemic sclerodema in 1966, 1973, 1980 and 1983 [10]. In 1985, alteration in skin microcirculation in diabetic patients was reported by Tooke et al. [38]. Video capillaroscopy enabled analogue or digital recording which is a light microscope with a stationary setup combined with a video camera and recording system [39, 40]. Figure 2.1 illustrates the setup of video capillaroscopy in use for nail fold microcirculation monitoring.

In 1981, fluorescent tracers were introduced for microscopic microcirculatory imaging to improve the image quality of videomicroscopy [41]. The system, fluorescence videomicroscopy, uses a fluorescence microscope instead of a regular microscope used in video capillaroscopy. Bollinger

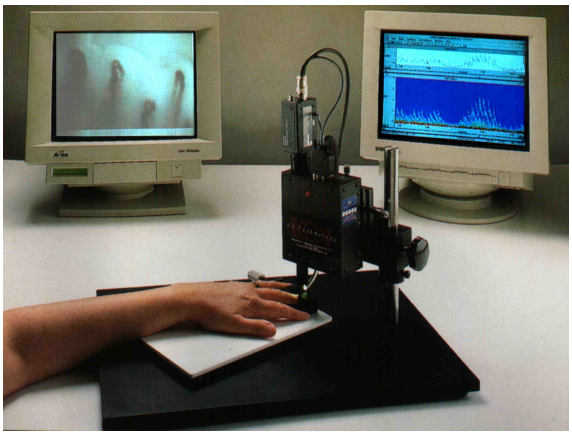

Figure 2.1: Nailfold video capillaroscopy (Photo courtesy of KKTechnology)

examined skin capillary diffusion in long-term diabetic patients using fluorescence videomicroscopy [42].

Laser Doppler Fluxmetry (LDF) is another imaging technique developed to visualize microcirculation. Bonner developed LDF using the knowledge of extended frequency of the scattered light when monochromatic laser light interacts with moving red blood cells [43]. Changes occurring in microcirculation due to chronic venous insufficiency and chronic venous ulceration have been investigated using LDF technology [44, 45].

Due to stationary setup of imaging devices, skin microcirculation and microvascular pathology related to chronic diseases remained the main focus of research until the early 21st century. Recently-developed hardware systems significantly contributed to study of human microcirculation [1, 39], providing novel tools to visualize capillaries close to the surface of the body [46].

In particular, the two major imaging modalities, Orthogonal Polarization Spectral (OPS) imaging [47] and Side-stream Dark Field (SDF) imaging [48] have been extensively employed in the field of clinical microcirculatory research. OPS imaging is a noninvasive method which does not use fluorescent dyes; instead it applies a video microscopic camera with light filtration [47, 22]. The optical schematic of OPS imaging technique is depicted in Figure 2.2.

OPS imaging uses green polarized light with wavelength of *550 nm* which is absorbed by hemoglobin and makes red blood cells visible [1]. Most of the polarized light is reflected back to the lens from the surface in the polarized form. Approximately %10 percent of the polarized

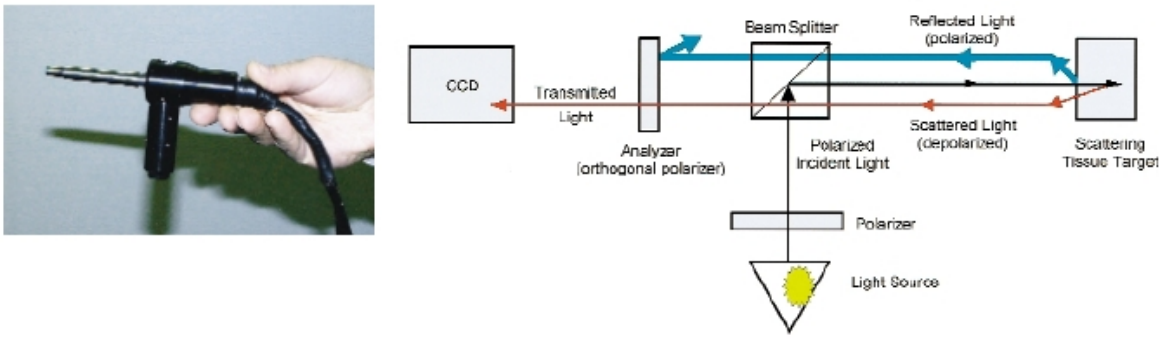

Figure 2.2: Orthogonal Polarization Spectral imaging probe and its optical schematic (Photo courtesy of Groner et al. [1]

photons pass into the tissue and become depolarized. The reflected polarized light is eliminated using an analyzer and depolarized light scattered in the tissue is allowed to pass through the analyzer. The depolarized light, then forms the microcirculation image on the Charged Couple Device(CCD) videocamera.

SDF imaging technique provides an improvement in image quality over OPS imaging and has been widely employed in the field of clinical microcirculatory research [49, 48, 50]. Light emitting diodes (LEDs) form a ring at the tip of a light guide. LEDs illuminate the tissue with green light of wavelength $540 \pm 50\ nm$ which is absorbed by hemoglobin. Interference of direct surface reflection is avoided by optically isolating the light source from the emission light path [2]. The schematic diagram of SDF imaging is presented in Figure 2.3.

Skin and sublingual microvascular beds are easily accessible to observe human microcirculation, therefore most of the clinical studies focus on nail-fold and sublingual microcirculation. Among mentioned imaging techniques nail fold video microscopy is used to visualize nail fold microcirculation whereas laser doppler technique allows skin, muscle, rectal, vaginal, and gastric mucosal blood flow to be monitored. OPS and SDF imaging techniques are mostly used to visualize mucosal surface microcirculation such as sublingual blood flow. These techniques can be utilized to visualize skin microcirculation in the areas with a thin epidermal layer such as eyelids [34].

Nailfold videomicroscopy is an easy and inexpensive imaging technique; however it may not represent microcirculation in other parts of body under certain circumstances such as cold environment. The disadvantage of laser doppler technique is that it can not measure the heterogeneity

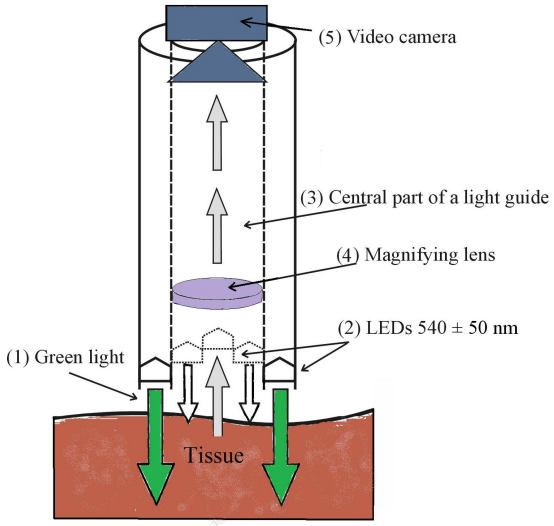

Figure 2.3: Schematic diagram of Sidestream Dark Field Imaging (Photo courtesy of Turek et al. [2])

of the blood flow. Motion artifacts caused by tongue and/or subject movement or movements as a result of respiration are main limitations of sublingual microcirculation imaging [34]. Therefore reducing the motion artifacts of microcirculatory videos is one of the main tasks for the proposed study.

To analyze microcirculatory images and videos several software tools have been developed. However currently available softwares are unable to perform real time analysis of the videos and require manual interventions. According to Awan [10]:

> "To facilitate routine clinical use, improved software should be developed."

In order to better see these shortcomings, some of these system tools are reviewed next.

CapImage was originally developed for traditional intravital microscopy [51], but is capable of analysis of SDF and OPS images [22]. It uses a Line Shift Diagram Method for measurement of velocity and real-time movement correlation. The software tool is capable of measuring properties of microcirculation such as blood cell velocity, capillary density, capillary diameter and capillary distance, vasomotion and area. However the software is only capable of detecting straight blood vessels. Expert users of CapImage claim that analysis of microcirculation with CapImage is time consuming and occurs off-line [52].

CapiScope, a system for the measurement of capillary morphology and capillary blood cell velocity, requires stable images and lacks stabilization [53]. JavaCap and Capilap toolbox are two other available software tools which use triangulation method to calculate intercapillary distance [54, 55].

Automated Vascular Analysis (AVA), which has been developed recently, is the most current commercial software tool for analyzing microcirculation videos. The methodology behind this software was described by Dobbe et al [56]. The method is the most accurate among the existing systems, performs a semi-automated process based on image stabilization, centerline detection and space time diagram. Despite all the capabilities provided by AVA, it lacks the full level of automation that leaves the burden of selecting the areas of interest, configuration, initialization, filtering of many false positives, dealing with many false negatives and addressing of connectivity to physicians/users. In addition, according to the developers of AVA, the software lacks the automatic vessel detection, as well as diameter and blood flow calculation [11].

For this study, video recordings are captured using a Microscan SDF imaging system from the sublingual surface of animal and human subjects. Over time, despite the advances in the hardware, the lack of effective computational methods to automate the analysis and interpretation of these videos, automation and speed have remained as the major challenges and obstacles in more widespread adoption of this valuable technology. Manual analysis is a tedious, slow and error-prone task which lacks accuracy. Most importantly, it prevents true point of care utilization of intravital microscopy.

Therefore, there is a need for a fully automated system that can:

- Stabilize microcirculation videos and eliminate motion artifacts
- Segment blood vessels within a specific range of diameter values
- Identify vessels with blood flow
- Quantitatively measure the level of tissue oxygenation via microcirculation using Functional Capillary Density.

Presented system can be specialized for other applications that require automated analysis of vascular images such as angiograms and retinal images. These vascular images are used in many

diagnostic decisions, and as such, the proposed system can help physicians which will significantly reduce the time of the decision making process and increase the accuracy of the decisions made.

2.1 Related Work for Digital Image Stabilization

Image stabilization is the process of generating a new video sequence by removing the unwanted motion between frames of the original video. The main causes of the motion are the shake of camera and subject movements. Image stabilization methods can be categorized in three groups: mechanical stabilization, optical stabilization and digital stabilization [57]. Mechanical stabilization techniques utilizes mechanical devices to keep the camera stable such as tripods and accelerometers. Optical stabilization approach changes the optical system of the device by detecting the motion using sensors and moving the sensor accordingly. Both approaches, mechanical and optical, develop techniques to stabilize the image before recording and both are hardware dependent [58] . Meanwhile digital stabilization is a software based approach and it is applied to the image after recording. Digital stabilization can be combined with mechanical and optical stabilization techniques.

The process of digital image stabilization can be divided into two major tasks: motion estimation and motion correction [59]. First unwanted motion is estimated and global motion vectors are calculated. Then corrections are applied to the frame sequence according to the global motion vectors. The nature of transformation to be estimated and corrected may vary depending on the application. Stabilization systems which focus only on translational motion effects are called two-dimensional (2D) stabilization systems, whereas three-dimensional (3D) systems deal with rotation and zoom based transformation along with translation [60, 58].

According to Jae Lim, motion estimation algorithms can be categorized in two main groups: region matching methods and spatio-temporal constraint methods [61]. Bit-plane matching [59], feature tracking, pyramidal approaches [62] and block matching [58] algorithms can be considered as the most commonly used region matching methods. Spatio-temporal approaches include direct optical flow estimation [63], phase correlation [60], integral projection [64] and least mean-square error matrix inversion [65] approach. Spatio-temporal approaches are superior to region matching algorithms in terms of computational time.

Feature tracking algorithms are widely studied among other regional matching methods. Stabilization algorithms track features such as points, lines and surfaces in the images to determine the global motion vectors. The features can be extracted from anatomical structures of medical images [66, 67] such as bronchial/vascular branches in the case of lung [68]. Geometrical features (e.g. local curvature extrema and corners) are used to estimate the translation of the images as well [69, 70]. Feature based methods are effective if the images contain enough distinctive and easily detectable objects. Unfortunately, medical images rarely provide many details and for this study, detecting the anatomic structure (blood vessels) is the main goal.

Algorithms that are based on image intensity values work differently. Image transformation is determined by optimizing pixel intensity similarity measurements. The similarity is calculated using cross-correlation, Fourier domain based cross-correlation, minimization of variance of intensity ratios, histogram clustering and minimization of histogram dispersion, and maximization of mutual information [71].

Block matching algorithms use a predefined size of windows-blocks or even entire images to estimate motion vectors. One of the disadvantages of block matching methods is defined as 'remarkableness' of the window content [72]. If a window does not contain distinctive details, there is a high probability of mismatch.

To stabilize microcirculatory videos, two different approaches are utilized separately. First, a block matching algorithm is developed that calculates cross-correlation coefficients to measure the similarity of the blocks. To avoid errors caused by 'remarkableness' issue, blocks are ensured to include blood vessels using Laplacian of Gaussian filtering. The accuracy of the stabilization algorithm is improved utilizing Lucas-Kanade optical flow to track the blocks selected. Lucas-Kanade optical flow is commonly used in literature for tracking purposes [73, 74]. Instead of calculating optical flow globally, Lucas-Kanade calculates local optical flow. Details are discussed under Chapter 6.

2.2 Related Work for Segmentation

Quantitative information on microcirculation can be derived by calculating the density of the microvessels within a field of view and can be used to monitor and assess the changes occurring in

tissue oxygenation and perfusion over time. To evaluate the density of the microvessels, segmentation of blood vessels is a necessary process. Vessel segmentation is a widely studied field in the various areas of biomedical image processing. Most of the existing vessel segmentation methods focus on retinal images [75, 76, 77]. There are a few studies working with angiographic images, ultrasound images and microcirculatory videos as well [78, 79, 56].

Several algorithms have been suggested to segment blood vessels. In 2004, Kirbas & Turek published a review of existing vessel detection algorithms [80]. They categorized the algorithms in six groups: pattern recognition based, tracking based, model based, neural network based and artificial intelligence based approaches and tube like object detection algorithms such as road detection algorithms from satellite images.

Pattern recognition techniques are concerned with the automatic detection of vessel structures and vessel features [81, 82, 83]. Multi-scale approaches, which are sometimes classified under pattern recognition techniques, use different resolution levels to extract different size of vessels.

Use of Gabor filters for multi-scale analysis of the images is very common among vessel detection algorithms. A feature vector is created from the properties of gabor filters and pixels are classified as vessel or non-vessel using different classification methods such as support vector machine (SVM) classifiers, Gaussian mixture models (GMM), k nearest neighborhood classifiers and neural networks (NN) [84, 85, 86]. Li et al. use adaptive tracking and morphological filtering followed by multi-scale analysis instead of feature extraction and classification [87].

Matched filters are widely used to extract vessels from retinal images [88, 78, 89, 90, 76]. The approach convolves images with various filters to detect the vessels with different orientation and size. Multiple kernels search for vessels at different directions and the maximum response of the kernels is retained. The large size of kernels drastically effects computational time.

Region growing algorithms start with a seed point and measures the similarity of adjacent pixels based on intensity values or other features [91, 92]. These algorithms reach high accuracy with homogeneous images or homogeneous regions of the images but fail to detect vessels in pathological or heterogeneous images.

Hessian matrix based approaches calculate the eigenvalues of the Hessian matrix and classify pixels accordingly [93, 94, 95]. The standard deviation of the Gaussian is used to estimate the

diameter of the vessels. Recent studies show a tendency towards Hessian matrix based methods [89].

One of the advantages of neural network based segmentation methods is that they allow the use of nonlinear classification. However most of the neural network based approaches require a training process in which a very large and representative training database has to be provided. Sinthanayothin et al. extract retinal blood vessels using multilayer perception neural net [96].

Morphological operators use the geometrical structure of the vessels [97, 98]. Morphological operators can be used to correct segmentation results, to fill holes or to remove isolated pixels as well. However, they usually require prior knowledge to extract blood vessels accurately.

Model based approaches, which include active contour models, basic and improved snake models and gradient vector flow algorithms use prior knowledge of vessels to match a model with the input image [99, 100, 101]. Although snake models are an improvement for these types of applications, still they require manual preliminary initialization which prevents automation. Snake approach seems to work well for thick blood vessels but it fails to detect capillaries, which is a major target of this research. Another constraint of snake models is that once it detects the vessel, the rest of segmentation is based on tracking the vessels.

Tracking-based approaches start with initial points known to be a part of blood vessel and apply local operators to the image to track vessels [102, 103, 79]. Vessel tracking methods that assure the connectivity of vessel segments provides reasonable performance for well-structured vessel images such as retinal images but are not considered suitable for noisy and irregular images such as microcirculatory frames. Another disadvantage of tracking based approaches is that they are not fully automated and often require user intervention for selecting start and end points.

The categorization of vessel segmentation algorithms vary in the literature. Florin et al. divide vessel segmentation algorithms into two groups [104]:

- Model-free algorithms: Hessian matrix based approaches, region growing algorithms, tracking based approaches, morphological operator approaches, and adaptive thresholding.
- Model based algorithms: Active contour models, snake models, geometric and parametric deformable models.

Jiang and Mojon proposed an algorithm based on adaptive thresholding in 2003 [105]. Their algorithms first applies thresholding to the image at different levels, then verifies the pixel as vessel at each level using the geometric features of the vessels.

Classifying the existing algorithms based on the need of supervision is another approach [94, 95]:

- Supervised methods: Neural network based approaches, K-nearest neighbor and Bayesian classifier based methods
- Unsupervised methods: Matched filters, adaptive thresholding, vessel tracking, snake models and morphology-based techniques

One of the well-known supervised vessel segmentation algorithms is proposed by Staal et al. [94]. Ridges, which correspond to the centerlines of the blood vessels, are extracted from the image based on Hessian matrix approach. Feature vectors are computed for each pixel based on the line elements. Manually labeled images are used to train the system and k-nearest neighbor classification is employed to classify the pixels.

Other common way of categorizing vessel detection methods is: Window based methods, classifier based methods and tracking based methods [84].

There are also studies combining two or more of the mentioned methods to detect blood vessels from medical images.

Although blood vessel segmentation is a widely studied area, there are not many studies on microcirculatory images. Most of the vessel detection approaches that have been discussed are rather case-based, semi-automatic or computationally expensive, which make them not applicable to the majority of clinical and research applications [80].

Regardless of their capabilities, the existing methods have several limitations that significantly limit their use in processing of SDF or OPS video recordings with poor local contrast. Some of the existing methods need initialization, while some others require prior knowledge and user interaction. Most of the existing techniques have difficulties detecting the edges and centerlines. Another limitation of the existing methods is that, while they may work fine for a single image, they require considerable computation time for processing of videos which are comprised of numerous consecutive image files.

This research focuses on fully-automated, close to real-time analysis of sublingual microcirculatory videos. The aim of segmentation process is to detect blood vessels whose diameters are within a specific range to ensure they belong to microcirculation and to identify capillaries with blood flow from segmentation results. Presented segmentation algorithm is adapted from Jiang and Mojon's multiple level thresholding algorithm [105]. Jiang's algorithm is capable of segmenting retinal blood vessels with high accuracy. However it fails to extract capillaries from microcirculatory videos. Therefore, the segmentation algorithm is improved to include pre-processing and post processing steps. The main algorithm is also modified to automatically compute the threshold range for each image sequence. The details of the segmentation algorithm are further discussed in Chapter 5.

Chapter 3

Proposed Method

In this chapter, an overall description of the proposed method for automated analysis of microcirculatory videos is provided. For this study, Microscan SDF imaging technology is used to capture video recordings from the lingual surface of animal and human subjects. Data are provided by School of Medicine of Virginia Commonwealth University and Reanimation Engineering Science Center of VCU (VCURES). Since SDF imaging technology allows observing capillaries only if red blood cells (RBCs) exist, RBCs bounded with vessel walls are considered as vessels.

The input of the proposed system is a microcirculation video of *'N'* of frames. The algorithm is divided into two main blocks: Video Processing and Image Segmentation as Figure 3.1 shows.

1. Video Processing-Stabilization: Microcirculation video is stabilized in the first step of video processing to remove motion artifacts. Two approaches are developed to stabilize video frames. The first approach calculates cross-correlation coefficients and applies block matching. The second approach utilizes Lucas-Kanade optical flow technique to track features throughout the video. Resulting stabilized video frames are averaged in time domain to eliminate discontinuity effect of vessels. The details of proposed algorithm are described in Chapter 6, under Stabilization section.

2. Segmentation: Time-averaged frames are given as input to the segmentation block. To segment vessels from averaged frames, first pre-processing is applied to enhance the contrast. Pre-processing is followed by thresholding. After thresholding frames at multiple levels, geometric operators are calculated. Pixels are classified as vessel or background using geometric operators and intensity values. Segmentation results from all threshold levels are then com-

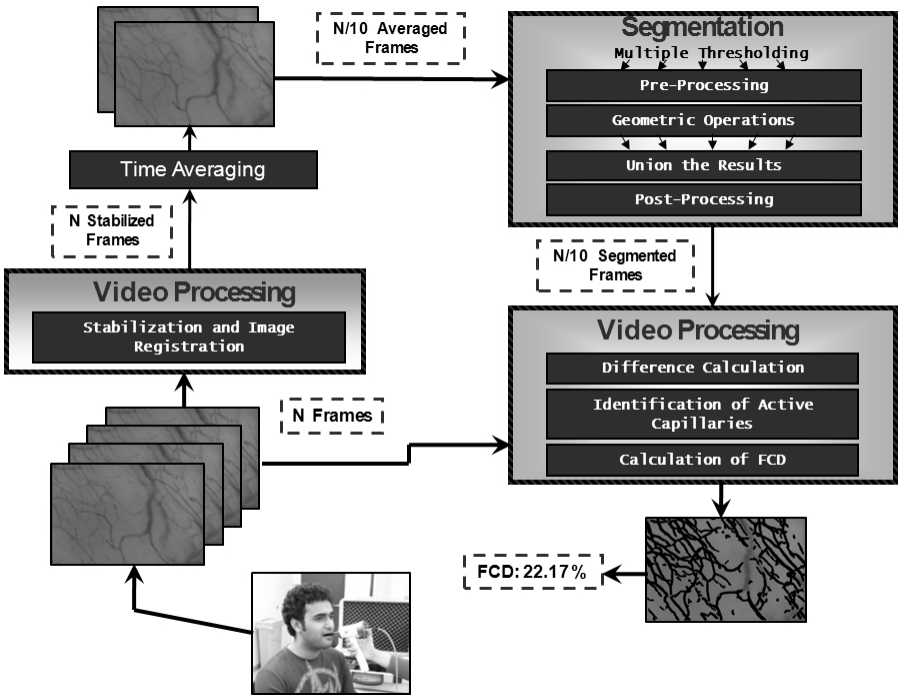

Figure 3.1: Overall schematic diagram of the proposed algorithm.

bined to generate one segmented binary image for one averaged frame. To eliminate discontinuity problems, a region growing algorithm is applied after segmentation. The segmentation methodology is discussed in details in Chapter 5.

3. Video Processing-Difference Calculation: To identify capillaries with blood flow, the difference of consecutive video frames are used as well as segmentation results. After identification of vessels with flow, Functional Capillary Density (FCD) is calculated for quantitative measurement of microcirculation. The details of difference calculation algorithm are provided in Chapter 6, under Difference Calculation section.

Chapter 4

Segmentation

4.1 Overview

In this chapter, the proposed image segmentation method is explained in detail. The chapter starts with describing the methodology of segmenting blood vessels in range of interest from microcirculation video recordings. The method includes three major steps: pre-processing, geometric operations and post-processing. The algorithm is applied to microcirculation video recordings and retinal images, and results are presented in Chapter 7.

4.2 Description of the Method

The proposed segmentation method is designed to extract blood vessels from microcirculatory video recordings with predefined geometric structure. The algorithm starts with contrast enhancement of the video frames during pre-processing. Enhanced frames are converted to binary images using multiple threshold levels and at each threshold level pixels are verified using geometrical operators. Finally, region growing algorithm is applied to resolve discontinuity of vessels. An overall schematic for the segmentation algorithm is presented in Figure 4.1. Prior to pre-processing, frames are averaged in time domain. Second step is pre-processing which is repeated for each threshold level with different parameters. Multiple threshold levels are created for further steps of the algorithm. Euclidean Distance Map is used to calculate geometrical operators such as diameter and angle of the vessels. Using geometrical operators and contrast level information, the pixels are classified as vessel or background. These steps are repeated for each threshold level. The resulting segmented

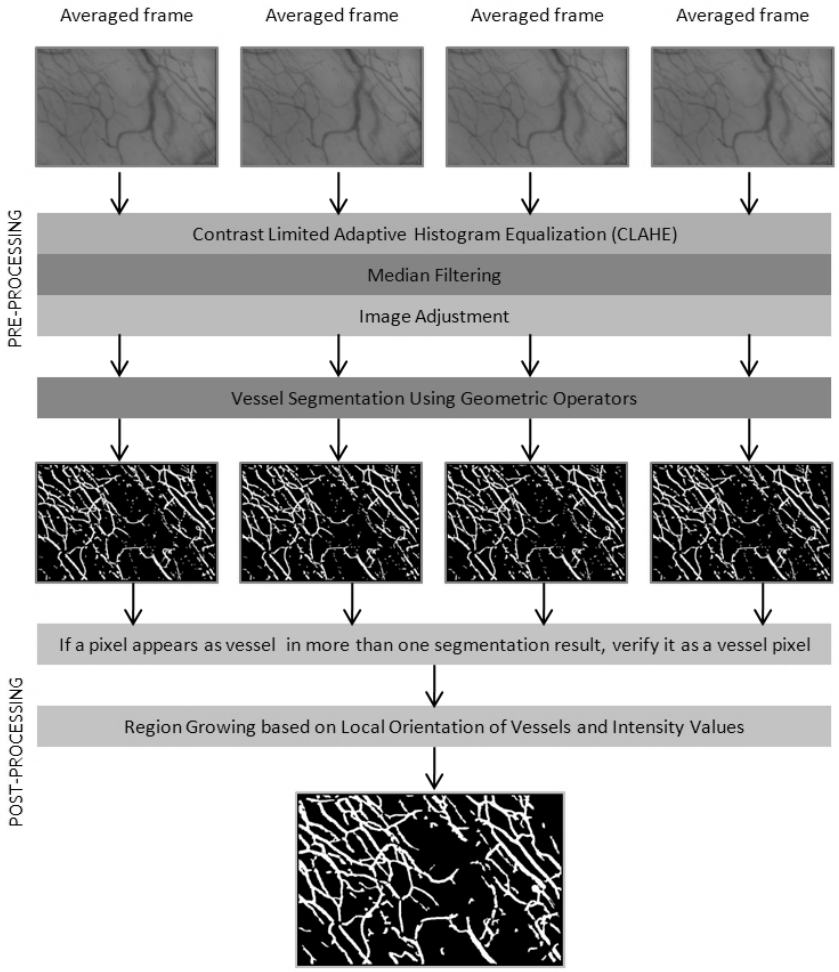

Figure 4.1: Schematic Diagram of segmentation algorithm.

binary images are combined for each averaged frame using OR operation. Region growing algorithm is developed using the orientation of vessels and contrast ratio as decision parameters.

4.2.1 Pre-processing

To improve segmentation accuracy, first low contrast microcirculatory video recordings are pre-processed. In order to reduce noise and identify capillaries as continuous structures, stabilized video recordings are averaged in time domain prior to pre-processing. The arithmetic average of intensity value for each pixel coordinate for a set of 10 frames is calculated and the intensity value of the current pixel is replaced by the calculated value.

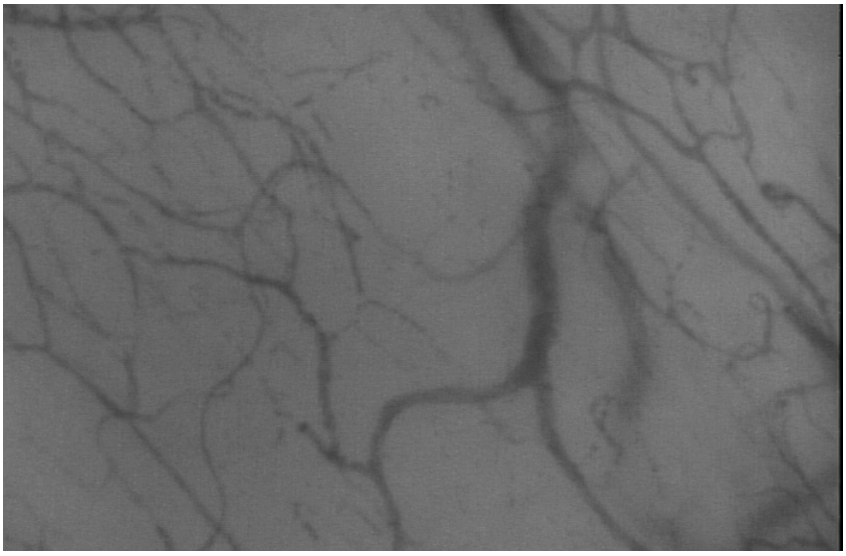

Figure 4.2: Original microcirculatory video frame captured from a healthy subject.

The original microcirculatory frame captured from a healthy subject is presented in Figure 4.2 before the time-averaging process. Figure 4.3 shows a time averaged microcirculatory video frame. In the original microcirculatory video, one can see the movement of individual red blood cells (RBCs) that construct continuous blood vessels in the averaged frames. As mentioned before, since hemoglobin is absorbing the green light from SDF probe, only the existence of RBCs makes the blood vessels visible.

Figure 4.4 presents a microcirculatory video frame captured from a hemorrhagic subject. The decrease in the visible blood vessels is apparent in the hemorrhagic subjects.

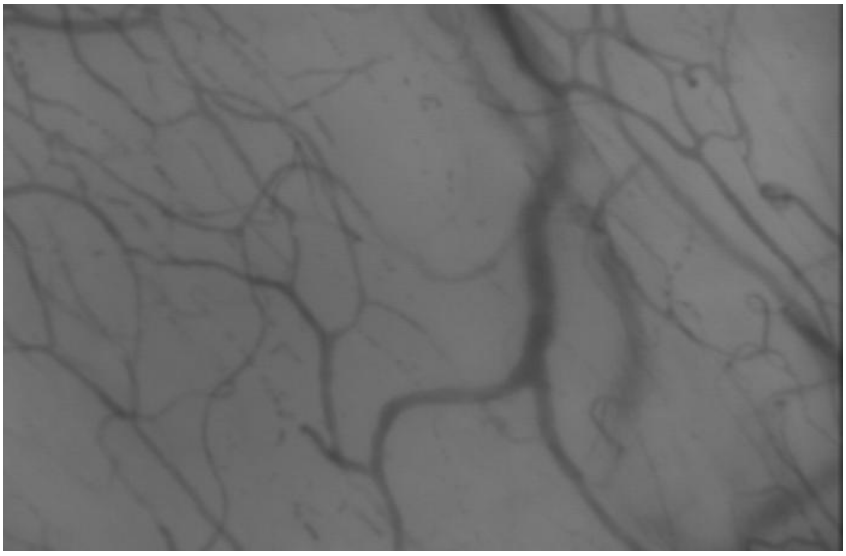

Figure 4.3: Result of averaging 10 frames from the microcirculatory video presented in Figure 4.2

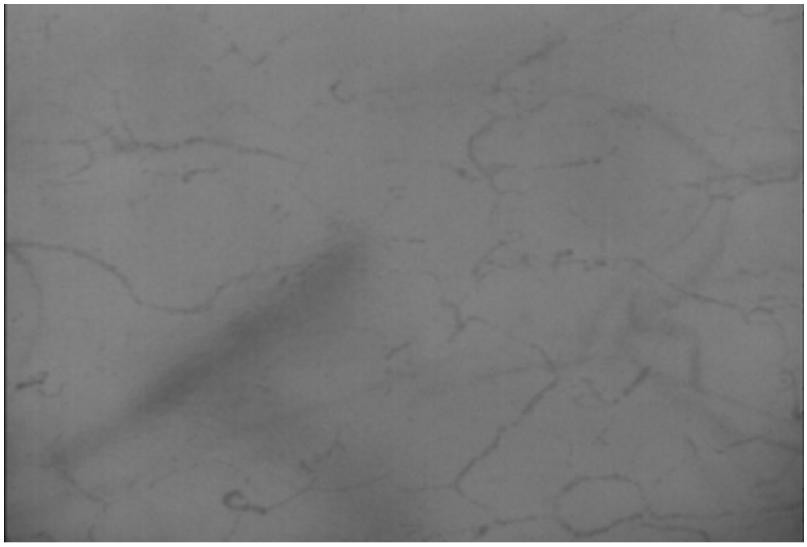

Figure 4.4: Original microcirculatory video frame captured from a hemorrhagic subject.

To enhance local contrast, Contrast Limited Adaptive Histogram Equalization (CLAHE) is performed on microcirculation images. CLAHE partitions the image into small regions, called 'tiles', and applies histogram equalization to each tile in order to even out the overall gray level distribution of the image [106]. Bilinear interpolation is then applied to eliminate boundaries of neighboring tiles. CLAHE differs from regular local histogram equalization by limiting the maximum slope of the grayscale transform function. By clipping maximum histogram count, a limit on the slope is ensured. CLAHE clips histograms exceeding 'clip limit' and redistributes evenly among all remaining bins.

The number of tiles for adaptive histogram equalization are changed at each threshold level. At low threshold levels, the resulting binary image consists of only wide and clear vessels. To have a clear image of wide vessels, histogram equalization is applied in smaller tiles. When the threshold level increases, the resulting is a darker binary image with almost all vessels and background included. Number of tiles for adaptive histogram equalization are increased to enhance the thinner vessels. Output of histogram equalization for the frame in Figure 4.3 is presented in Figure 4.5. The contrast has been enhanced after applying histogram equalization and blood vessels have become more distinctive. Figure 4.5(a) is a result of histogram equalization with tile size '3'. The emphasis is given to wide vessels in this image. To generate Figure 4.5(b) the tile size of CLAHE is increased to 10. Contrast enhancement is focused on smaller vessels in this image.

The histograms of the original image and the image after CLAHE function are displayed in Figure 4.6.

Histogram equalization is followed by median filtering. To remove noise, median filtering is a widely preferred method in the literature. In this application, the purpose of applying median filter is to smooth the images. Median filter searches for the median value of neighboring pixels and replaces each pixel with the median value. The size of the filter is changed at each threshold level. For a low threshold value, where only wide and apparent vessels are preserved, the size of the filter is kept large. Since the details are not passing the threshold, the smoothing effect is much stronger at these threshold levels. With increasing the threshold value, the size of the filter is reduced to enable the details pass through the thresholding process.

Finally image adjustment is applied to the output of median filtering. To adjust images, the

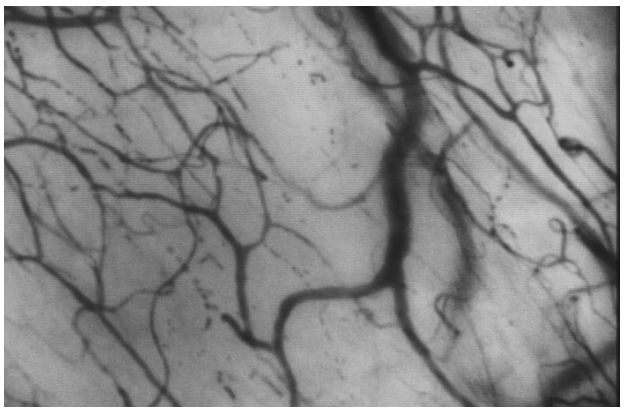

(a) CLAHE for tile size of 3

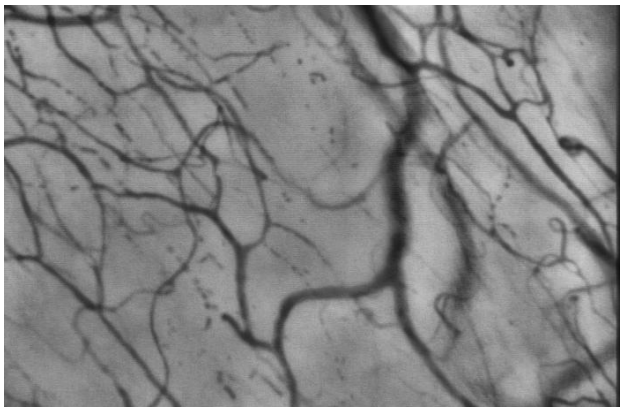

(b) CLAHE for tile size of 10

Figure 4.5: Result of adaptive histogram equalization (CLAHE) for Figure 4.3 at Threshold 1 and Threshold 10.

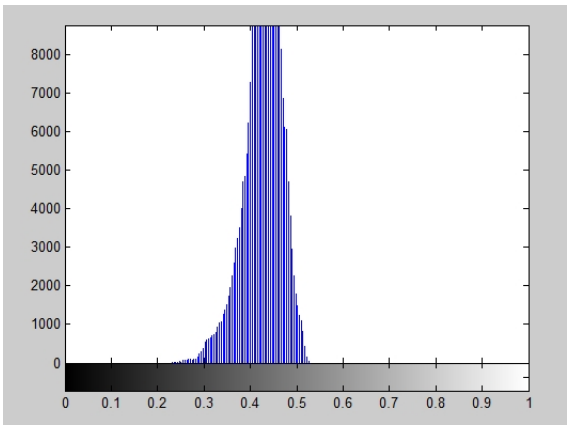

(a) Before CLAHE

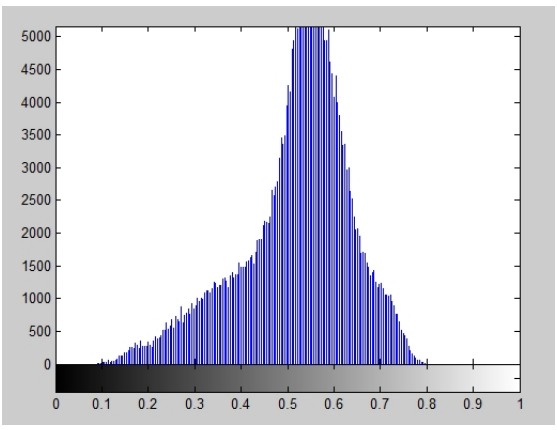

(b) After CLAHE

Figure 4.6: Histogram of the original image on the right, histogram of the image after CLAHE on the left.

contrast of the median filtered image sequences is stretched. The effect of image adjustment on the histogram of the images can be seen in Figure 4.7. The histogram in Figure 4.7(a) belongs to the output image of median filtering. The histogram in Figure 4.7(b) is after applying adjustment and the histogram is spread over the entire area.

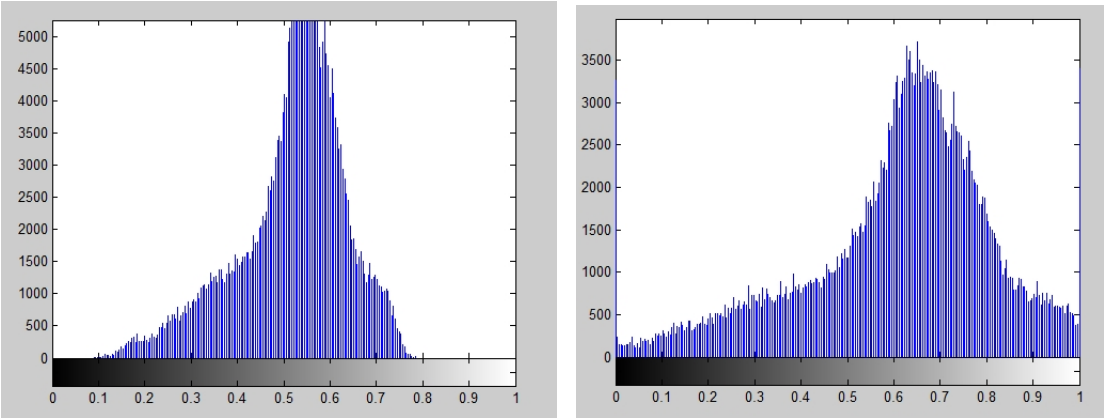

(a) Before image adjustment (b) After image adjustment

Figure 4.7: Histogram of the median filtered image on the right, histogram of the image after image adjustment on the left.

The outputs of pre-processing step are presented in Figure 4.8 for two different threshold levels. Smoothing effect of median filtering is evident in Figure 4.8 when it is compared to Figure 4.5. For the first threshold level, smoothing is more effective since the algorithm is focused on extracting only the wide and explicit vessels at this step. The effect of smoothing is reduced gradually to enable detecting of vague and thinner vessels at higher threshold levels.

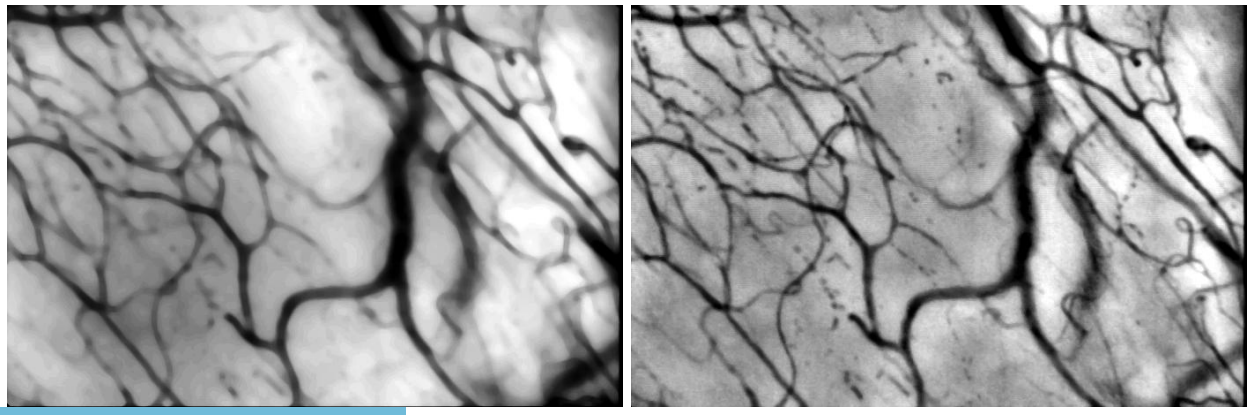

(a) At Threshold T_1 (b) At Threshold T_{10}

Figure 4.8: Pre-processed images for the first and last threshold levels.

Figure 4.9 provides a detailed diagram of the pre-processing and geometric operations steps for a single averaged frame. This process is repeated for each 10-block averaged frame.

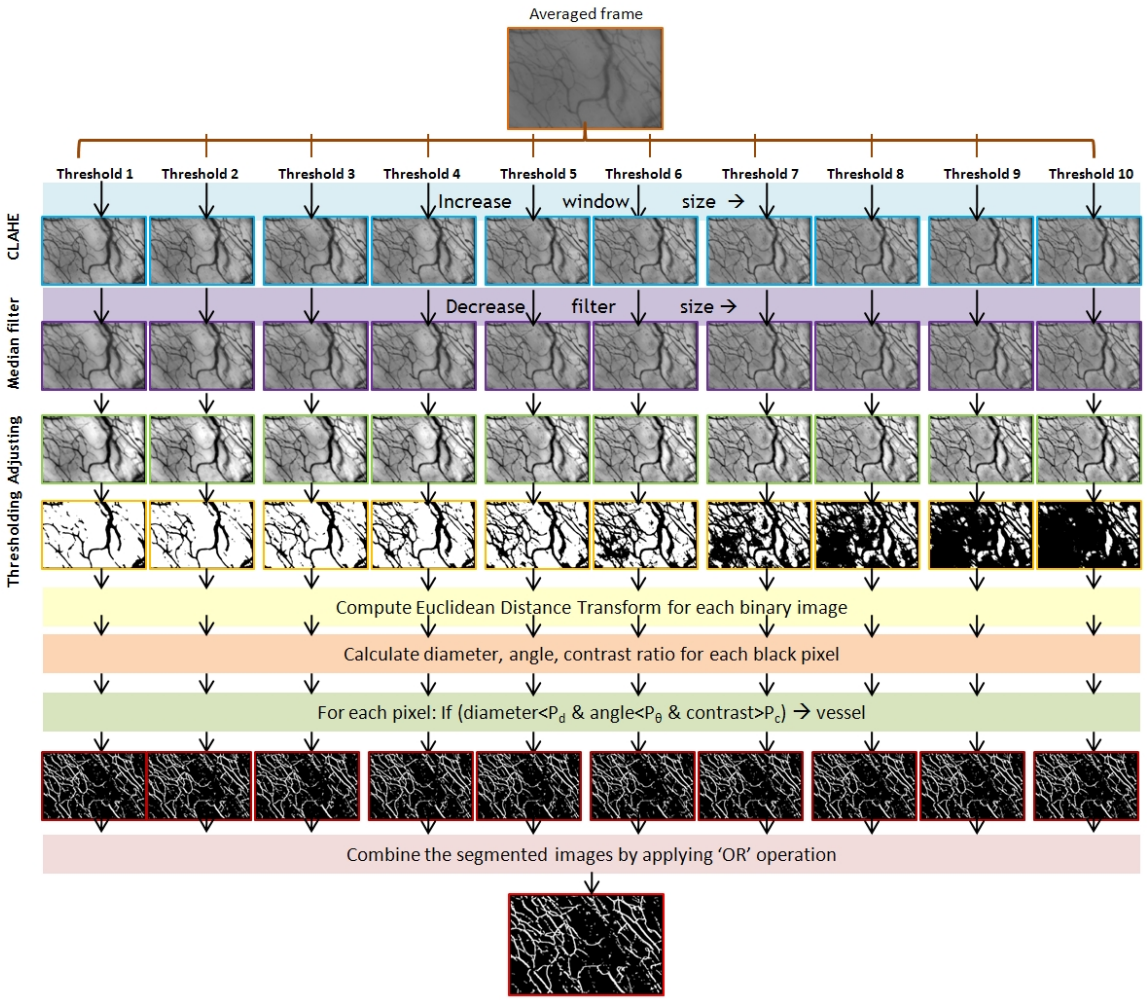

Figure 4.9: Detailed Diagram of pre-processing and geometric operators for one averaged frame.

4.2.2 Geometric Operations

Blood vessels are detected by using geometric operators to verify each pixel at multiple threshold levels as vessel. First, the pre-processed frames are converted to binary images using multiple threshold levels, which results in a number of binary images for each set of averaged frames. Ten threshold levels are applied to each pre-processed image. One default threshold range does not work properly for each image sequence. Since the intensity varies a lot among microcirculatory images,

applying a default threshold range results in multiple completely dark or completely white binary images. Instead, the threshold levels to be applied are computed based on the image characteristics. The histogram is used to decide the threshold levels. After averaging and histogram equalization process, the histogram of the image is calculated. Threshold range is based on the peak value of histogram, i.e. the gray level with highest number of pixels. Two sets of threshold ranges are defined and one is chosen according to the peak value of the histogram.

Figure 4.10 presents the result of thresholding at two different threshold levels; $T_1 = 89$ and $T_{10} = 204$ in a range of $[0, 255]$. The vessels passed the threshold in Figure 4.10(a) are only a few; whereas, in Figure 4.10(b) most of the background pixels are allowed to pass through. The threshold level is kept high to be able to catch every detail in the image. By calculating geometrical operators, wide vessels and background noise will be removed.

(a) At Threshold T_1

(b) At Threshold T_{10}

Figure 4.10: Converted binary images at the first and last (10th) threshold levels.

Morphological opening operator is applied to the binary images before the pixel verification process. Opening function removes all the objects with an area of less than pre-defined value. In the binary image it removes the connected components which have fewer pixels than P_{size}. At this step objects occupying less than 20 pixels are removed by morphological opening operator. A binary image before and after opening is shown in Figure 4.11. The red dots in the right image present the removed objects by opening function.

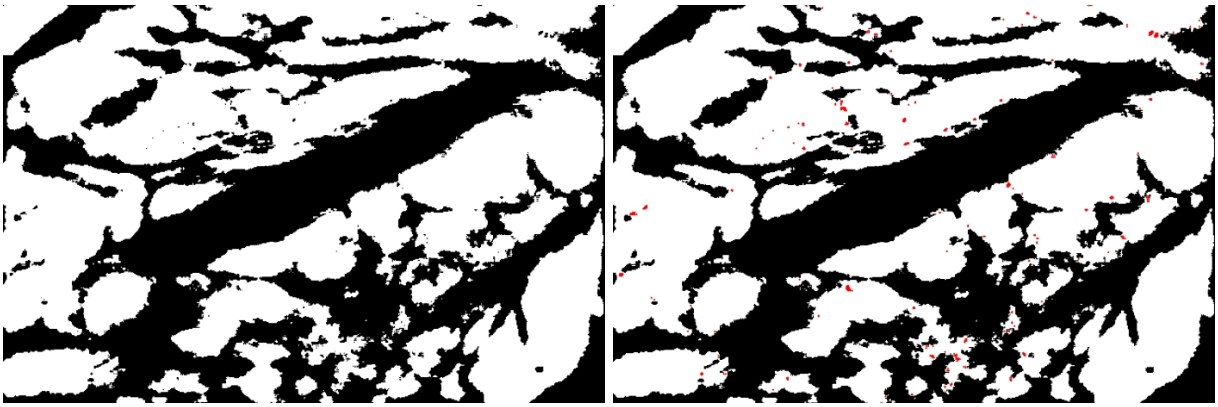

(a) Before opening (b) After opening

Figure 4.11: A binary image before and after morphological opening operation.

The methodology of pixel verification is modified from the retinal vessel extraction method proposed by Jiang and Mojon [105]. At each threshold level, two dimensional Euclidean Distance Transform (EDT) is calculated for the binary image. Distance Transform (DT) calculates the distance to the closest background pixel for all the pixels in an image. The calculation of the distance may change according to the distance metric such as 'euclidean', 'manhattan' or 'chessboard' distance. The metric used for this research is euclidean distance.

The formulation of EDT can be described as follows: From a binary image composed of an object O and background B, the result of EDT is an image, in which the value of any object pixel O is the distance from this pixel to the nearest background pixel B. If I is the binary image and pixel p belongs to an object in the image located at (i, j), i.e. $p = I(i, j)$, the general formula of 2-D EDT will be:

$$D(i,j) = min\left\{\sqrt{(x-i)^2 + (y-j)^2};\ p \in O,\ I(x,y) \in B\right\} \tag{4.1}$$

For background pixels, Euclidean Distance Transform value is '$zero$'. For $M*N$ size binary

image as an input, EDT produces two $M*N$ size matrices. The first matrix consists of the euclidean distance value to the closest background pixel for object pixels and '$zero$' for background pixels. The second matrix has the coordinate information of the closest background pixel b_p for the current pixel p. There are several approaches to compute EDT. Sequential Signed Euclidean Distance transform [107] is easy to implement and time efficient, however; it generates drastic numerical errors for large distance values [108]. Meijster's algorithm is used for this research, because of its efficiency in terms of computational time, accuracy and simplicity [109, 108].

Meijster's algorithm is based on independent scanning. First the algorithm scans each column separately for the nearest background pixel and generates one dimensional distance transform.

$$G(i,j) = min_y \left\{ (j-i)^2 ; I(i,y) \in B \right\} \tag{4.2}$$

Calculated 1-D DT, G, is used to generate 2-D DT based on parabola intersection concept. The details of Meijster's algorithm can be found in the original article [109].

The two outputs of EDT, distance values and coordinates of the nearest background pixels are used to calculate geometrical features of vessel candidate pixels. For each pixel of each binary image, three different features are calculated using the outputs of the map and the intensity values of the pixels. The process of verifying pixels according to the geometric parameters relies on the curvilinear structure of blood vessels. The diameter d and angle θ values of pixels are geometrical features of blood vessels. The gray level intensity values of the images after histogram equalization are used to calculate C, contrast ratio. Figure 4.12 is a detailed illustration of these geometrical parameters.

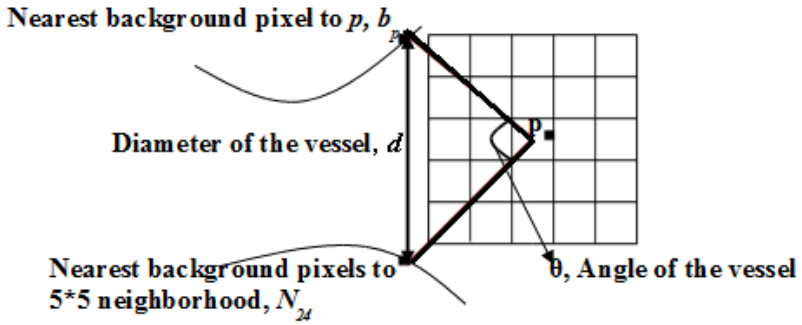

Figure 4.12: Descriptive graph of geometric parameters; diameter and angle.

Figure 4.12 describes the calculation of parameters in a 5*5 neighborhood. The current pixel is referred to as p, which is a vessel candidate; its 24 neighbors are shown in the figure. The nearest background pixel of p is b_p and the nearest background pixels to its 24 neighbors are N_{24}. Euclidean distance values between the background pixel b_p and 24 nearest background pixels N_{24} are computed and the maximum is decided to be the diameter for the pixel:

$$d = {}_{max} \left\| \overline{b_p, N_{24}} \right\| \tag{4.3}$$

'θ' is the angle between the background pixels b_p, N_{24} and center pixel 'p' according to Figure 4.12. The angle is calculated using the cosine rule:

$$\theta = {}_{max} \arccos \left(\frac{\left\| \overline{p, b_p} \right\|^2 + \left\| \overline{p, N_{24}} \right\|^2 - d^2}{2 \left\| \overline{p, b_p} \right\| \left\| \overline{p, N_{24}} \right\|} \right) \tag{4.4}$$

The maximum angle derived from 24 neighbor pixels is used as θ. The third feature is the ratio of gray level values of nearest background pixels and the vessel candidate p:

$$C = {}_{max} \frac{GL(N_{24})}{GL(p)} \tag{4.5}$$

where $GL(p)$ is the gray-level intensity value of current pixel 'p'. To calculate contrast ratio, images with enhanced contrast are used. Therefore, GL in Equation 4.5 stands for the gray level of the output of histogram equalization (CLAHE).

Finally, to verify the vessel candidate, three constraints are applied: d needs to be less than pre-defined P_d to avoid large vessels, θ needs to be larger than P_θ to ensure curvilinear structure is kept and the calculated contrast ratio needs to be higher than P_c. If the pixel in the binary image is not background ($p \in O$), and it meets the criteria defined by three parameters P_d, P_θ and P_c, it is verified to be a vessel pixel. In other words; if $p \in O$ in thresholded image and:

$$d(p) < P_d \;\; \& \;\; C(p) > P_c \;\; \& \;\; \theta(p) > P_\theta \tag{4.6}$$

p is verified as a vessel pixel. The same procedure is repeated for all object pixels of all threshold levels. In the end, for one time-averaged frame input, there will be NT segmented images where NT is the number of threshold levels. To eliminate false positives, the pixels which are verified as vessels in more than one segmentation result are saved as vessel pixels.

The parameters, P_d, P_θ and P_c are selected after multiple experiments. P_d controls the diameter of the blood vessels to accept. It is determined based on the diameter of blood vessels and capillaries

to be included in microcirculation. P_θ is another geometric parameter to ensure curvilinear structure of the vessels and is empirically derived.

Experiments showed that the contrast ratio, which is controlled by P_c, varies significantly not only across different videos, but also across different regions of the same frame. Therefore, an adaptive methodology is generated to decide on the local value of P_c for each video. In Figure 4.13 two frames from different microcirculation videos are depicted. The contrast ratio between vessel and background is low in Figure 4.13(a), which shows variations across videos/frames. In addition, the upper side of the frame is darker resulting lower contrast ratio. This indicates the variations within a frame. In Figure 4.13(b) the contrast ratio is higher with respect to Figure 4.13(a) but this time the flare on top right corner causes the vessels to practically disappear.

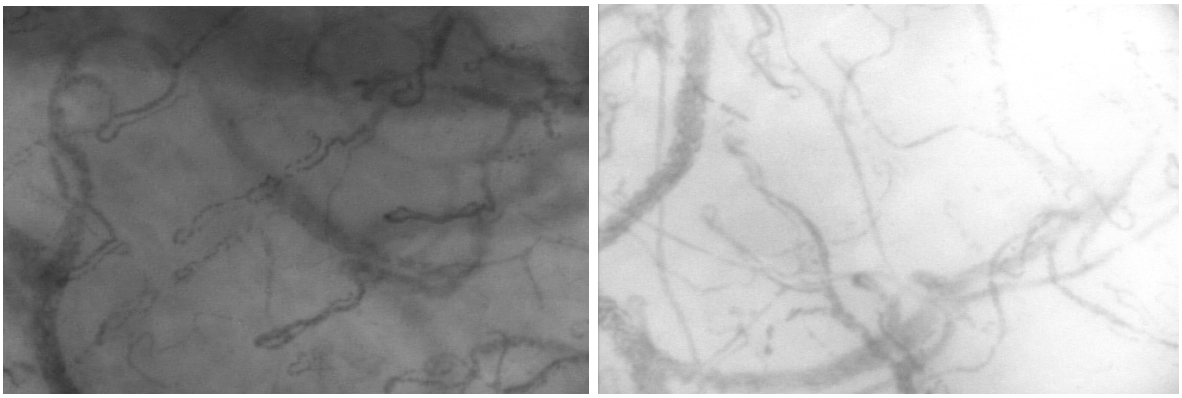

(a) A dark frame with uneven lighting

(b) A brighter frame with higher contrast ratio between vessel and background

Figure 4.13: Two frames from different videos presenting inconsistent contrast ratio between vessel and background.

Next, the adaptive strategy of selecting local P_c values is described. The histogram of a typical frame extracted from a microcirculation video shows two peak values that can be classified as vessel and background. Figure 4.14 represents two Gaussian models. Histograms of three different videos and extracted gaussians are displayed in Figure 4.15. The adaptive strategy estimates the distribution of the background and vessel regions in each frame and uses these local distributions to select the best local P_c.

The two mean values for vessel and background are calculated using maximum likelihood estimation of Gaussian mixture model by utilizing expectation maximization algorithm. After averaging and applying CLAHE, the image is divided into $75 * 75$ windows. The divided image is presented

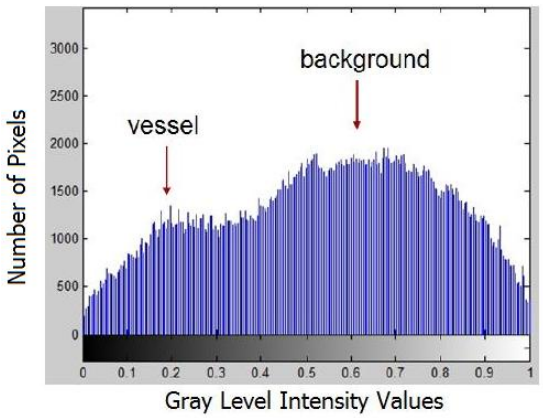

Figure 4.14: Histogram of a microcirculation video after histogram equalization used for Gaussian mixture model.

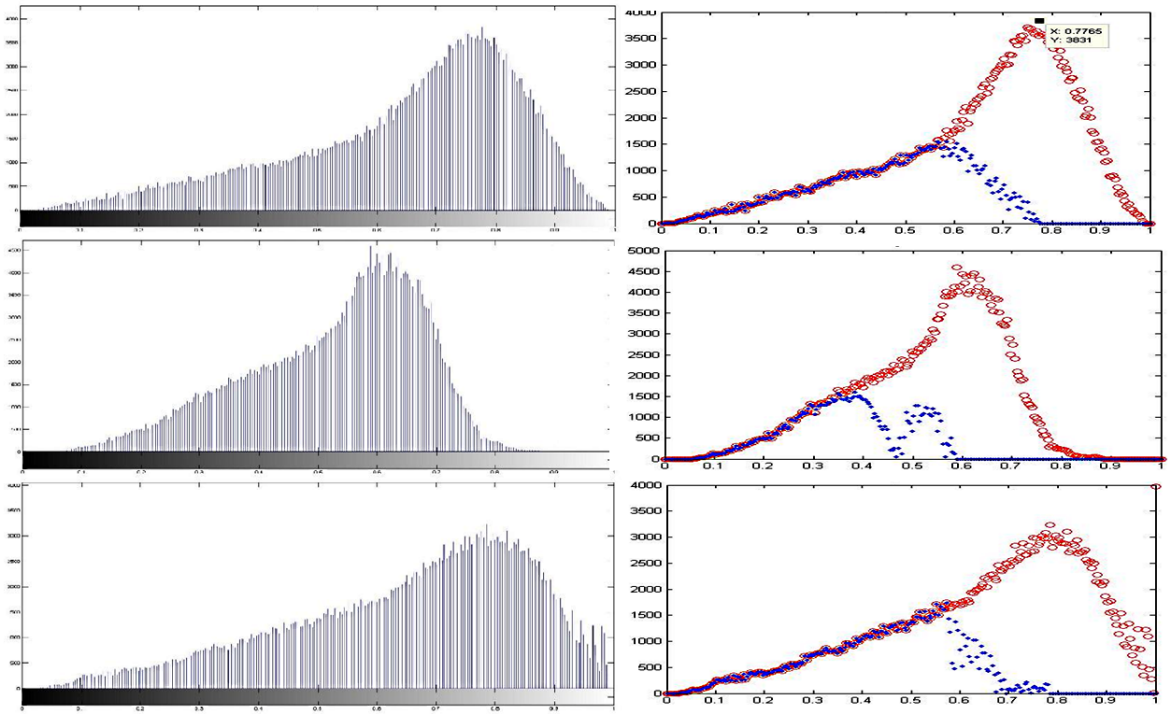

Figure 4.15: Histograms from 3 different videos with 2 Gaussian models highlighted in the histograms

in Figure 4.16. This window size is selected after a process of trial and error, testing sizes ranging from $50 * 50$ to $100 * 100$. For each window, the mean values are estimated with expectation maximization (EM) for Gaussian mixture models (GMM). The aim of the expectation maximization algorithm is to optimize the likelihood that the given gray level values are generated by a mixture of two Gaussian s. It consists of two major steps and iteratively alternates between these steps: expectation and maximization [110]. The algorithm starts with randomly initializing the parameters to be estimated. In the expectation step, the expected value of log likelihood is calculated given the data and current estimation. In the maximization step, it re-estimates the parameters by maximizing the expected value log likelihood function.

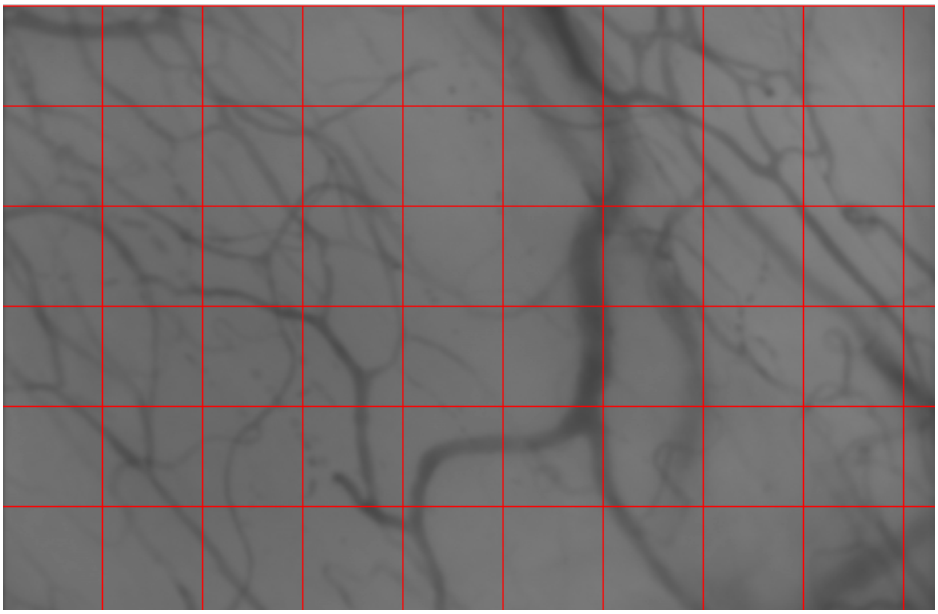

Figure 4.16: Microcirculatory frame divided into $75 * 75$ windows.

The parameters estimated through EM algorithm are the mean of the intensity of vessel pixels and the mean of the intensity of background pixels for each $75 * 75$ window. Two different P_c values that give acceptible segmentation results when applied globally are used for these windows. 100 acceptible segmented windows are used for training. Using simple k-means clustering, a decision rule is generated based on the mean of the intensity of the background pixels. For each window, if the estimated mean of background pixels (m_1) is lower than 0.7, $P_c = 1.55$ is chosen. For the estimated mean of background pixels higher than 0.7, i.e. $m_1 > 0.7$, $P_c = 1.7$ gives better segmentation results. This way, for bright and dark windows different P_c values are used. The

value 0.7 is calculated using direct application of a clustering technique, i.e. K-means, on the data.

Two P_c values for dark and bright windows do not extract all the vessels of interest accurately. To improve the accuracy further, a second rule is generated based on the estimated mean value of vessel pixels (m_2) in the window. First, the window is classified as dark or bright based on the estimated mean of background pixels, m_1. Then, the estimated mean value of vessel pixels m_2 is checked to decide the contrast ratio between vessel and background for the current window. The following expert system rule set, in the form of pseudo-code describes the process:

```
for each window
if m1<0.7
     if m2<0.22
        Pc=Pc2;
     else
        Pc=Pc4;
     end
     else
     if m2>0.4
        Pc=Pc3;
     else
        Pc=Pc1;
     end
  end
end
```

For each 75∗75 window in the frame, one of the four P_c values is selected based on the two estimated mean values, m_1 and m_2.

4.2.3 Post-processing

Since the segmentation algorithm is based on pixel verification, it is possible to have isolated pixels in the result. To prevent that, binary morphological operators are used. Morphological opening operator is utilized to eliminate objects including pixels with $P_{size} \leq 20$. By using diagonal filling operation, holes within the segmented vessels are filled. The gaps between segmented components are filled by applying morphological 'bridge' function. Bridge function sets background pixels '0' to '1' if they have two $1 - valued$ neighbor pixels that are not connected. Figure 4.17 illustrates how diagonal filling and bridge operators work.

The effect of diagonal filling on black and white images is shown in Figure 4.18. The left side

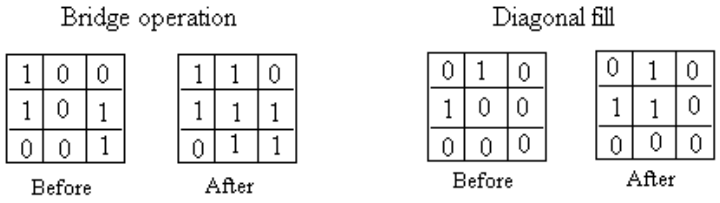

Figure 4.17: An illustration for morphological diagonal filling and bridge operators.

image is before the diagonal filling operation and the right image is after the operation.

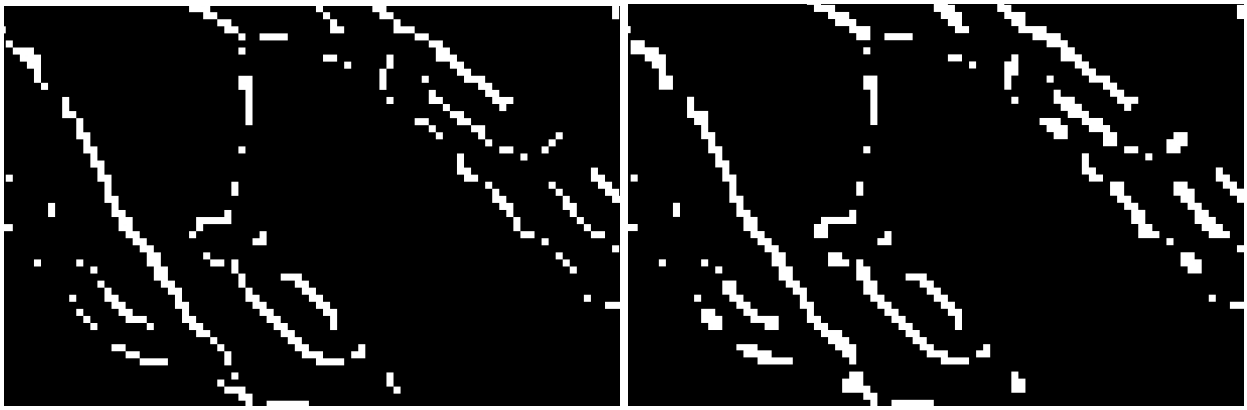

(a) Before filling (b) After filling

Figure 4.18: Result of morphological diagonal filling in a binary image: Before and After.

Then, the morphological 'bridge' operation is applied to the binary image on the right of Figure 4.18. The result of bridge operator is presented in Figure 4.19.

Furthermore, a region growing algorithm is developed to overcome disconnectivity of blood vessels. First, the final segmented image is divided into $35*35$ windows to determine the orientation of segmented vessel within the window. The vessel is allowed to grow in the computed direction if the gray level is within the range of average gray level of vessel pixels in the window $\pm 0.5*$ *standard deviation*.

4.3 Summary of Novelties

- Pre-processing: A novel pre-processing method is presented that changes the number of tiles for contrast limited adaptive histogram equalization and the size of median filter at each threshold level.

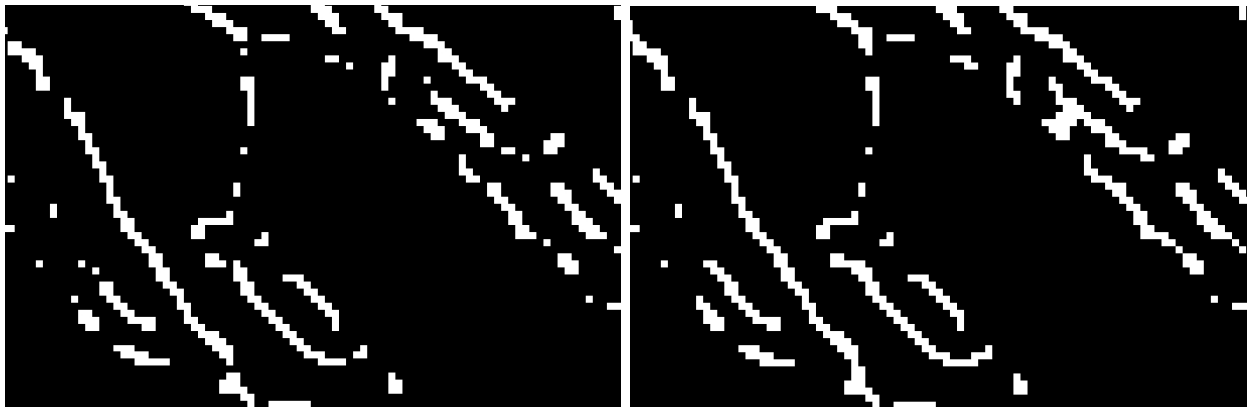

(a) Before 'bridge' (b) After 'bridge'

Figure 4.19: Result of morphological bridge operation in the binary image: Before and After

- Local P_c: A rule-set is generated using machine learning algorithms to adaptively select local P_c values based on statistical properties of local region in microcirculatory videos. The local adjustment of P_c value with using machine learning is a significant novelty that affects the quality of results.

- Region Growing: In post-processing, a novel region growing algorithm based on the orientation of blood vessel is presented in a pre-determined window.

Chapter 5

Video Processing

5.1 Overview

In this chapter, the Video Processing methodology is described. Video Processing algorithm consists of two main parts: Video Stabilization and Difference Calculation. Video Stabilization algorithm is applied to the videos to eliminate motion artifacts. After segmenting all blood vessels, difference calculation method is utilized to identify capillaries with blood flow.

5.2 Description of the Method

Video Processing algorithm contains two separate sections: Stabilization and Difference Calculation. Two different algorithms are developed to stabilize microcirculatory video recordings. The first method uses block matching approach and maximizing cross-correlation coefficients. The second method calculates optical flow using pyramidal implementation of Lucas Kanade. In the second part of video processing, difference of consecutive frames are calculated to identify blood vessels with flow. Then, quantitative measurements of microcirculation such as Functional Capillary Density (FCD) are calculated using active blood vessel information.

5.2.1 Video Stabilization

For video processing applications, stabilization is a necessary step to eliminate motion artifacts occurring due to the movement of subject and/or device. Microcirculation video recordings used for this study are subject to motion artifacts because the camera is not mounted and it is not easy

to hold tongue still during the capturing process of the SDF video. As such, significant stabilization effort has to be made at the image processing level. Image stabilization algorithms can be analyzed in two basic steps:

- Estimate the motion
- Motion correction transform

To estimate the motion, local motion vectors are generated from subregions of the image, called 'blocks'. To generate local motion vectors, statistical features of the subregions can be used such as mean absolute difference. Cross-correlation coefficients are used for that purpose. The global motion of a frame needs to be determined to correct motion by processing these local motion vectors.

The main idea of first stabilization method is maximizing cross-correlation coefficients for the areas that are known to include vessel pixels. Gaussian Gradient filtering is applied to enhance images and to improve visibility of blood vessels. The overall diagram of this stabilization algorithm is presented in Figure 5.1.

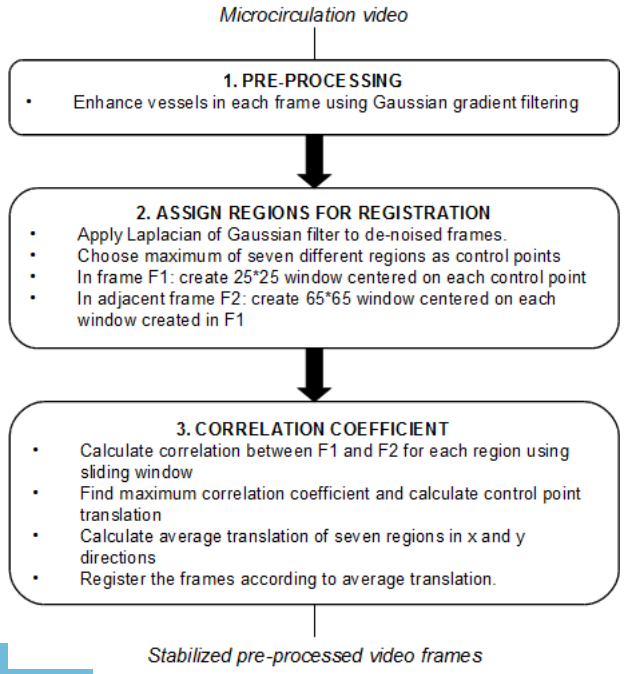

Figure 5.1: Schematic diagram of stabilization algorithm.

The blood vessels in the video frames are much darker than background and can be characterized by a large and sudden change in gray-level intensity of the pixels; in other words, a large and sudden change in the gradient. Gaussian gradient filtering is widely used in image processing applications. A two dimensional Gaussian kernel is applied to smooth the images and first order derivative of the results is calculated in x and y direction, i.e.:

$$G(x, y, \sigma) = \frac{1}{2\pi\sigma^2} e^{-\frac{x^2+y^2}{2\sigma^2}} \tag{5.1}$$

where x and y are the coordinates of the pixel and σ is the standard deviation factor, a parameter identifying the width of the filter. The kernel's degree of smoothing is determined by the standard deviation σ, which is $\sigma = 2$ for this study. Then, the derivatives in both x and y directions are calculated:

$$GD(x) = \frac{\partial G(x, y, \sigma)}{\partial x} = \frac{\partial \left(\frac{e^{-\frac{x^2+y^2}{2\sigma^2}}}{2\pi\sigma^2} \right)}{\partial x} = -\frac{x}{\sigma^2} \frac{e^{-\frac{x^2+y^2}{2\sigma^2}}}{2\pi\sigma^2} \tag{5.2}$$

$$GD(y) = \frac{\partial G(x, y, \sigma)}{\partial y} = \frac{\partial \left(\frac{e^{-\frac{x^2+y^2}{2\sigma^2}}}{2\pi\sigma^2} \right)}{\partial y} = -\frac{y}{\sigma^2} \frac{e^{-\frac{x^2+y^2}{2\sigma^2}}}{2\pi\sigma^2} \tag{5.3}$$

The magnitudes of $GD(x)$ and $GD(y)$ are added together to compute Gaussian gradient of the image. Gaussian gradient in x and y directions for the image in Figure 4.3 are presented in Figure 5.2.

$$GG(x, y) = |GD(x)| + |GD(y)| \tag{5.4}$$

The edges of blood vessels will appear bright against a dark background in the resulting image. After adding the magnitudes in both directions, the final result of Gaussian Gradient is shown in Figure 5.3.

One downside of the block matching algorithms is 'remarkableness'. Distinctive features of the images are selected and assigned as control points to overcome remarkableness issue. Control points are selected which are known to belong to capillaries to calculate the transformation between two consecutive frames. For this purpose, Laplacian filter is applied to the output of Gaussian Gradient. Laplacian filter is a $3*3$ filter which calculates second order derivatives. In the presented algorithm,

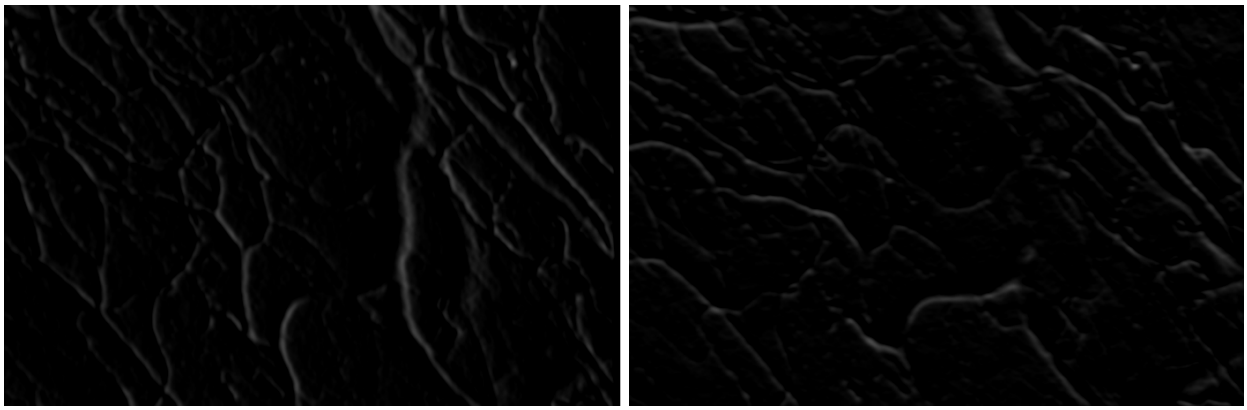

(a) Gradient of x (b) Gradient of y

Figure 5.2: Gaussian gradient of the image in x and y directions.

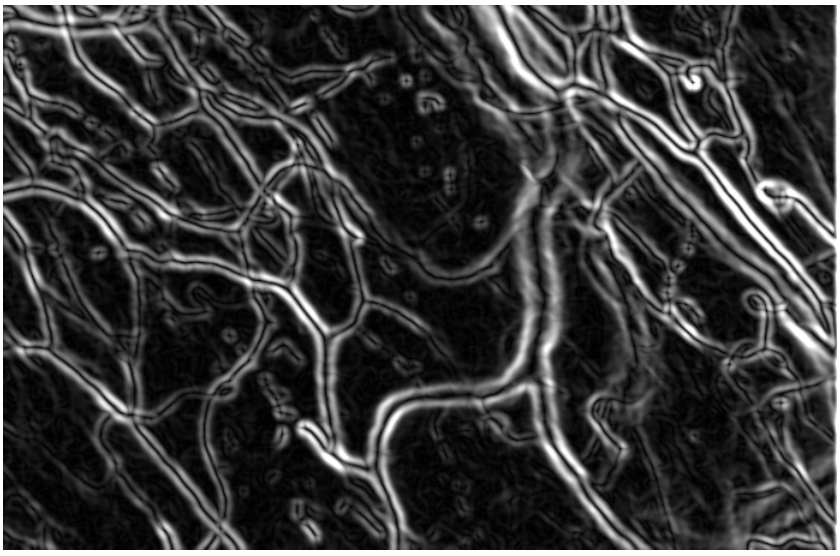

Figure 5.3: Gaussian gradient filtered image.

second order derivative of filtered image $GG\,(x,y)$ is calculated using the formula:

$$\nabla^2 GG = \frac{\partial^2 GG(x,y)}{\partial x^2} + \frac{\partial^2 GG(x,y)}{\partial y^2} \tag{5.5}$$

Using Equation 5.5, a $3 * 3$ filter is created as follows:

$$\nabla^2 = \frac{4}{(\alpha+1)} \begin{bmatrix} \frac{\alpha}{4} & \frac{1-\alpha}{4} & \frac{\alpha}{4} \\ \frac{1-\alpha}{4} & -1 & \frac{1-\alpha}{4} \\ \frac{\alpha}{4} & \frac{1-\alpha}{4} & \frac{\alpha}{4} \end{bmatrix} \tag{5.6}$$

The α parameter is used to control the shape of Laplacian filter and $\alpha = 0.8$ for this research. The output of Laplacian filter is shown in Figure 5.4. The vessel centerline pixels have higher intensity values in the resulted image.

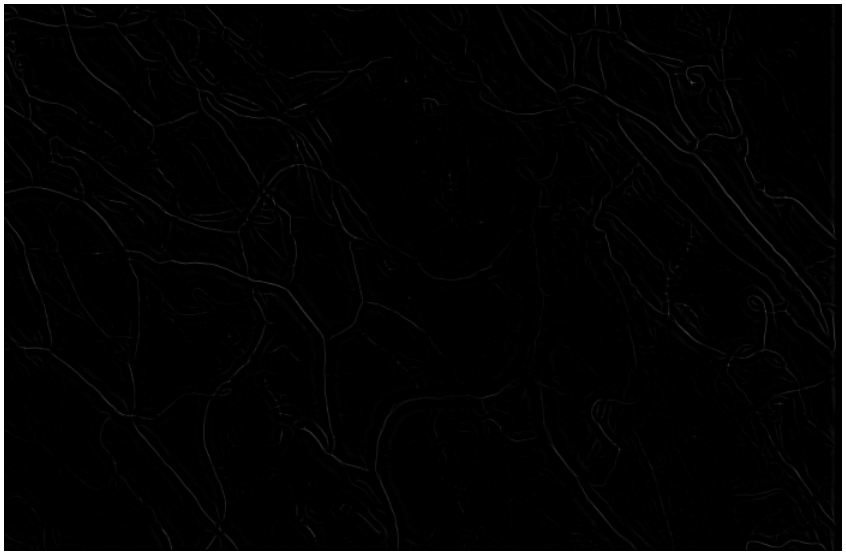

Figure 5.4: Output image of Laplacian filter.

Figure 5.5 shows the graphics of gray levels for the original frame, Gaussian Gradient of the same area and result Laplacian of Gaussian filter. A vessel between x coordinates 15 and 20 results a drop in gray level of original frame.

It can be seen from Figure 5.5 that the centerline of the vessel results as a local maxima in gray level of the output image of Laplacian filter. Therefore, maximums of the resulting filtered image are used to select the control points to make sure control points are part of vessel centerlines. Seven control points are defined at the first frame and they are tracked through consecutive frames. From

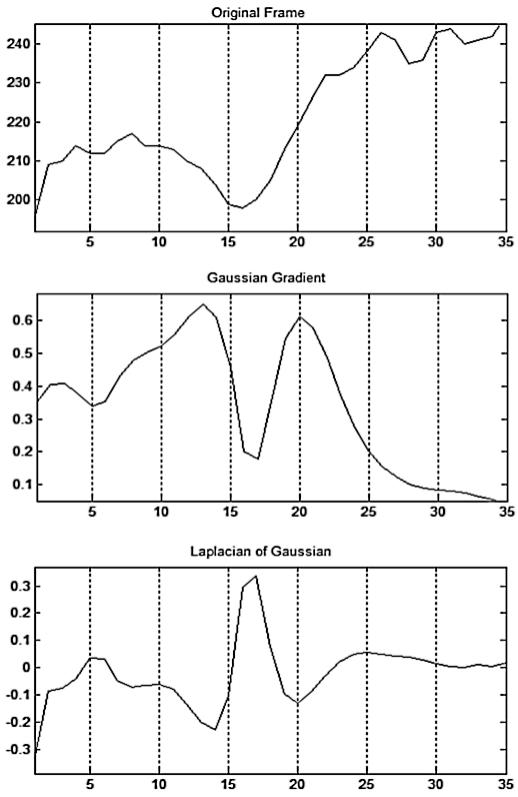

Figure 5.5: Graphics of a horizontal line where a vertical vessel exists.

seven control points, four of them are selected around four corners of the first frame. Other three are selected from the mid-area. Since control points are tracked throughout the video, selecting them is not repeated at each frame. Only if any of the defined control points leave the current frame, new control points are defined using the same method. The seven control points selected for the sample image in Figure 4.3 are all on the blood vessels as it is shown in Figure 5.6.

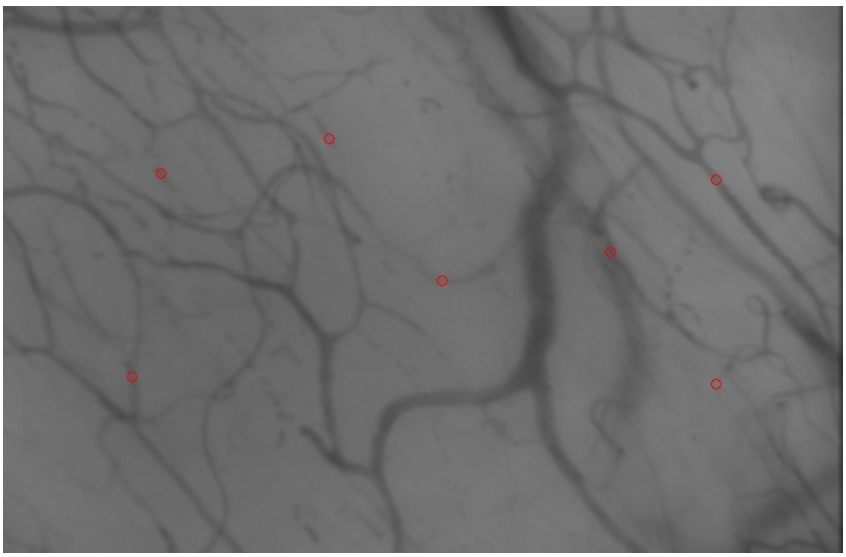

Figure 5.6: Seven selected control points from the local maximums of Laplacian filtered image

To calculate cross-correlation coefficients, sub-areas are defined using the control points as centers of the areas. A larger region around defined sub-areas is scanned and maximum correlated region is found. A detailed figure is presented in Figure 5.7 to get a better understanding. From the first frame, a region with an area of 25*25 is defined around the selected control points. These regions are shown in white rectangles. From the consecutive frame, an area of 65*65 around the 25*25 region is used to slide windows which is shown with rectangles in black. A 25*25 window is slided in the 65*65 region in the second frame and cross-correlation coefficients between the sliding window and the region from the first frame are calculated for each sliding window.

Cross-correlation coefficients between two regions from consecutive frames are calculated using Equation 5.7:

$$R\left(f_1, f_2\right) = \frac{C\left(f_1, f_2\right)}{\sqrt{C\left(f_1, f_1\right) C\left(f_2, f_2\right)}} \tag{5.7}$$

In the equation, f_1 is one of the green regions from the first frame and f_2 is a $25 * 25$ sliding window from the pink regions in the consecutive frame. The variable C is the covariance matrix calculated

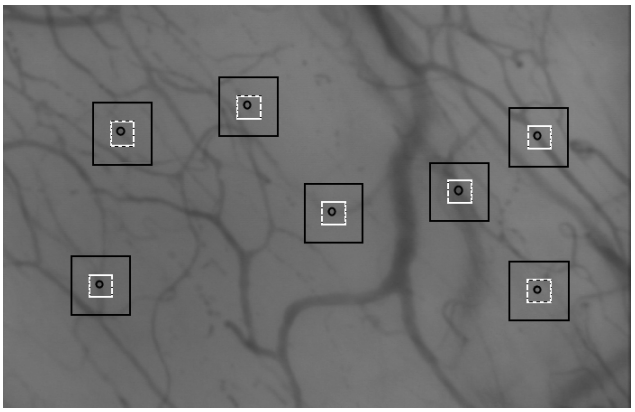

Figure 5.7: Seven regions from the first frame in green and scanned regions from consecutive frame in pink to calculate cross-correlation

by using the expected value E and $\mu_i = E[x_i]$:

$$C(f_1, f_2) = E[(f_1 - \mu_1)(f_2 - \mu_2)] \tag{5.8}$$

The window that gives the highest correlation coefficient is found for each region. The coordinates of highly correlated windows are used to calculate the displacement of seven regions. Displacement of current frame with respect to the previous frame is calculated by averaging displacement of seven regions both in x and y directions. First the displacement is calculated between the first and second frames. Then the frames are updated therefore for each frame the displacement is calculated according to the previous frame, not according to the first frame.

As mentioned above, in some of the video files, the motion of the camera is indeed so large that the tracked vessels leave the frame. When dealing with such frames, it is important to know if the frames are in transition to be able to track the vessels accurately. Using the displacement of frames and calculating the amount of change at displacement for a couple of consecutive frames, the frames are classified as 'in transition' or 'stable'. If the total amount of displacement for current frame, previous two frames and next two frames is higher than 15 pixels, current frame is labeled as 'in transition'.

As a second approach for stabilization, Lucas-Kanade method is used to compute optical flow. Lucas-Kanade optical flow algorithm is first proposed by Lucas and Kanade in 1981 as an image registration method [111]. The aim of Lucas-Kanade algorithm is to register a template image to an input image. To compute optical flow, the template image will be the image in time t_1 and the

input image is the image in time t_2. The algorithm finds the optical flow by minimizing the sum of squared error between the images I_{t_1} and I_{t_2}:

$$Error\left(I_{t_1}, I_{t_2}\right) = \sum_{x=1}^{M}\sum_{y=1}^{N}\left(I_{t_1}\left(x,y\right) - I_{t_2}\left(x,y\right)\right)^2 \tag{5.9}$$

M and N refer to the width and height of the images in this equation. If the image in time t_2 is the result of displacement of I_{t_1} in x and y directions, $I_{t_2}(x,y) = I_{t_1}(x+d_x, y+d_y)$, the error function to be minimized in Equation 5.9 will be:

$$Error\left(I_{t_1}, I_{t_2}\right) = \sum_{x=1}^{M}\sum_{y=1}^{N}\left(I_{t_1}\left(x,y\right) - I_{t_1}\left(x+d_x, y+d_y\right)\right)^2 \tag{5.10}$$

The goal of Lucas-Kanade optical flow algorithm is to find d_x and d_y that minimizes the error function in Equation 5.10. It starts with an estimation of d_x and d_y and iteratively solves the problem to find minimum sum of squared error. The algorithm calculates the displacement d_x and d_y for a number of pixels selected from the image and tracks them all along the video. The pixels to be tracked down are selected using the control point selection method described for the previous cross-correlation algorithm. 20 local maximums of Laplacian filtered image are used as features to make sure tracked pixels are all part of blood vessels. To compute Lucas-Kanade iteratively, pyramidal implementation of Lucas-Kanade is used as suggested by Bouguet [112].

Bouguet's algorithm first builds pyramidal representations of both images I_{t_1} and I_{t_2}. Pyramidal representations are simply images with lower resolutions. If I_{t_1} is an image of $640 * 480$, the first pyramidal representation of I_{t_1} will be an image of $320 * 240$ which is created from I_{t_1}. Initially, the displacement at the lowest level is assigned as zero and is used to calculate the displacement in the upper level. At each level, the calculated value from the previous level is used. After the pyramidal computation reaches to the top level which is the original image, the error function is minimized by iterative calculations.

The displacement vector for x and y directions from 20 points are then averaged to find the global motion vector. The frames are then aligned to the first frame accordingly.

5.2.2 Difference Calculation

After stabilization process, blood vessels in the range of interest are segmented from the stabilized video frames using the segmentation method described in the previous chapter. Segmentation of one microcirculation video will result in multiple segmented frames; one segmented frame for each 10-block averaged frame. The vessels in the range of interest are defined using geometrical parameters such as diameter and angle in the segmentation algorithm.

In the microcirculatory videos, some of the blood vessels appear without blood flow. However, to calculate microcirculation parameters such as Functional Capillary Density (FCD) vessels with blood flow are needed to be extracted. To identify blood vessels and capillaries with blood flow, further analysis is required. For that purpose, two parameters are calculated:

- Difference of gray level intensity values throughout the video for each pixel
- Segmentation results of the microcirculatory video

Difference of gray level intensity values between consecutive frames are calculated from the raw video. Summation of absolute differences for each pixel is used to determine the variability of gray level of each pixel:

$$S(i,j) = \sum_{k=1}^{N-1} |D(i,j,k)| \tag{5.11}$$

where $D(i,j,k)$ is the difference of gray level intensity values.

$$D(i,j,k) = I(i,j,k+1) - I(i,j,k) \tag{5.12}$$

N is the number of frames, k is the frame number, $I(i,j)$ is the current pixel from the original video.

Vessels with no flow will exist in all segmentation results because the red blood cells are not moving in the vessel throughout the entire video. Vessels with flow may also exist in all segmentation results since movements in individual frames are averaged using time-averaging before segmentation. Therefore there is a need to use a second parameter, which is the sum of differences in Equation 5.11. A weight function is defined using the sum of differences and vessels exist in all segmentation

results to identify capillaries with flow. If the pixel is verified as vessel in all segmentation results and the change of gray-level value of the pixel is below a determined threshold value 'ST', it is labeled as a '*no flow*' pixel:

$$NF(i,j) = \alpha\,(S(i,j) < ST) + \beta R(i,j) \tag{5.13}$$

ST is the mean value of the sum of differences in intensity value: $ST = \mu(S(i,j))$. $R(i,j)$ is set to '1' if current pixel is segmented as vessel for all averaged frames. If $NF(i,j)$ is '1', the pixel at i,j is decided to be a vessel pixel without flow. The parameters, α and β are chosen in such way to ensure that they add up to 1, i.e. $\alpha + \beta = 1$.

For each segmented vessel component in the video, if percentage of no-flow pixels is higher than 50% of the all pixels representing that specific vessel, then the vessel is classified as no flow. Otherwise it is identified as an active vessel.

To be able to measure microcirculation quantitatively, Functional Capillary Density (FCD) is calculated as suggested in a round table on evaluation of microcirculation [11]. The exact definition of FCD is as follows:

$$FCD = 100 * \frac{\text{total area of blood vessels with flow}}{\text{total area of the frame}} \tag{5.14}$$

FCD can be calculated either manually or by using computer software. The manual method involves gridding the video frame and counting the number of vessels that cross the lines of the grid, while the software method calculates the ratio of perfused vessels to the total surface.

5.3 Summary of Novelties

- Stabilization: The second stabilization algorithm which combines significant region selection strategy with Lucas-Kanade optical flow is a novel approach that reduces the computational complexity of the conventional Lucas-Kanade method and speeds up the algorithm. The points to be tracked in the proposed variant of Lucas-Kanade algorithm are selected to ensure that they all belong to capillaries.
- Difference Calculation: An automated novel algorithm is presented to identify blood vessels and capillaries with blood flow by calculating the difference of consecutive frames.

Chapter 6

Results

The presented algorithm is applied to microcirculatory videos provided by Virginia Commonwealth University, Department of Emergency Medicine. The vessel segmentation algorithm is tested on publicly available retinal image database as well.

6.1 Results for Microcirculation Video Recordings

The SDF microcirculation video recordings used for this research were captured from human and animal subjects by Virginia Commonwealth University, Department of Emergency Medicine. Virginia Commonwealth University Reanimation Engineering Science Center (VCURES) participated in sample preparation as well as FCD scoring of most of the videos. The width of about $4 - 5\mu m$ in a typical capillary appears around 3 pixels wide in such videos. The Microscan system has a disposable microscope tip, which is placed gently on the tissue. It guarantees a fixed distance of around 1 mm. The system has a point spread function of Gaussian distribution with standard deviation (SD) of around 1 pixel in x and y directions. The device records frames at a rate of 29 frames per second. Video files are captured from the surface of the tongue.

6.1.1 Results of Video Stabilization

The stabilization algorithm is applied to the microcirculation video recordings captured by Microscan SDF System. Stabilization algorithm is capable of classifying frames according to the amount of motion. The proposed algorithm proved to accurately identify frames in transition where the 'scene' is changing, i.e. when the motion is so much that almost a different area of

the tongue is being recorded. To verify the results of image registration, difference of consecutive frames are calculated before and after registration. Using non-parametric Wilcoxon test [113], it was verified that the proposed registration process significantly decreases the difference of adjacent frames (p-value of less than 0.0001).

6.1.2 Results of Vessel Segmentation and Identification of Vessels with Blood Flow

Two different sets of microcirculatory videos were analyzed. The first set is captured from animal subjects. There are eight video files in this group. Out of eight video files, four of them are from hemorrhaging swine subjects and the remaining four are from healthy subjects.

The video recordings are stabilized using the proposed stabilization algorithm, explained in detail in Chapter 6. Then, the videos are averaged in time domain and blood vessels with diameter less than 25 μm are segmented. An original frame from a healthy subject and segmented vessels and capillaries of the same frame are presented in Figure 6.1 and Figure 6.2.

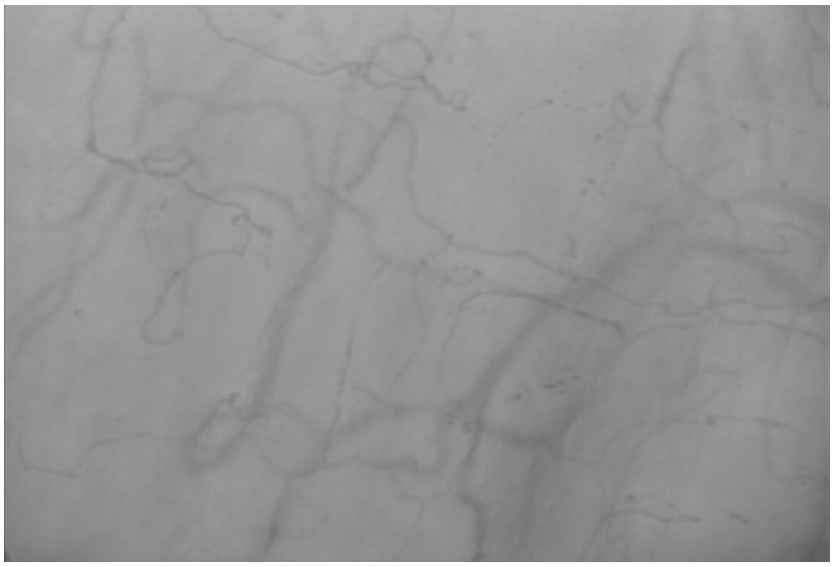

Figure 6.1: Time-averaged microcirculatory frame captured from the lingual surface of an healthy swine.

At this step of the algorithm, all blood vessels in the range of interest are segmented. Vessels with blood flow are identified later.

A microcirculatory video frame from a hemorrhagic subject is shown in Figure 6.3. There is

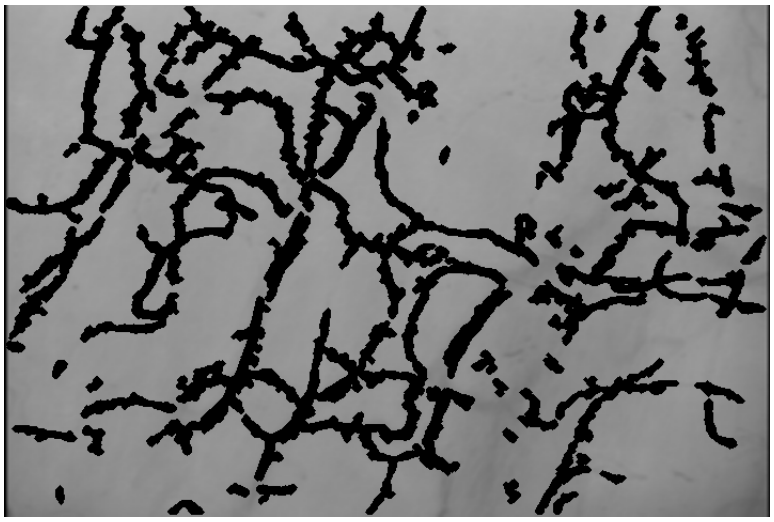

Figure 6.2: Result of vessel segmentation algorithm for Figure 6.1.

a visible reduction in the number of blood vessels. Since the number of RBCs is reduced as well, the contrast level of blood vessels are much closer to background making the segmentation process difficult.

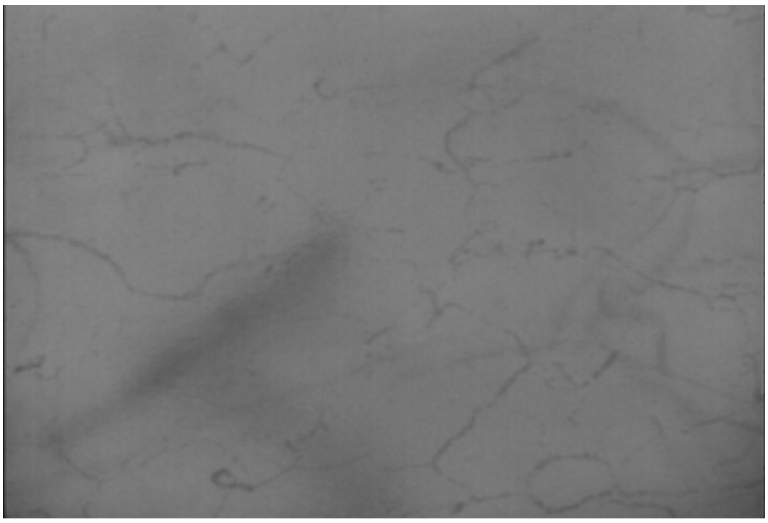

Figure 6.3: Microcirculatory video frame of a hemorrhagic swine subject.

The blood vessels and capillaries from the frame of hemorrhagic subjects are segmented and resulting image is illustrated in Figure 6.4.

After the segmentation process, the videos are analyzed further to identify active capillaries and to calculate Functional Capillary Density (FCD) values. Resulting FCD values for normal and

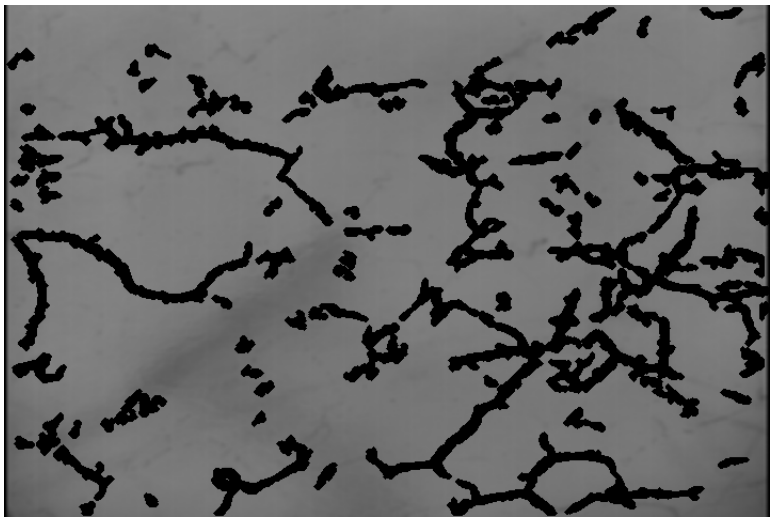

Figure 6.4: Segmented vessels of the frame of hemorrhagic subject.

hemorrhagic swine subjects are provided in Table 6.1. Most of the video files are recorded for more than 10 seconds, which results to about $\sim$ 300 frames. In each video, the first twenty frames are used to calculate FCD values. FCD values reported by experts were not available for this dataset, therefore the comparison is made in between healthy and hemorrhagic subjects only.

Table 6.1: FCD Results for Eight Subjects

Subjects	**FCD** %
Healthy 1	14.89
Healthy 2	17.24
Healthy 3	13.4
Healthy 4	16.48
Mean	**15.50**
Hemorrhagic 1	11.24
Hemorrhagic 2	4.25
Hemorrhagic 3	4.99
Hemorrhagic 4	10.5
Mean	**7.75**

The second dataset consists of human sublingual microcirculation videos. The recordings are from Intensive Care Unit (ICU) patients who were accepted with heart failure problems. Sublingual microcirculation videos of the patients are recorded at different time periods during their stay at ICU. Eight physicians analyzed the recordings using commercially available software AVA. Since the software lacks of the capability to identify active capillaries (i.e. capillaries with blood flow)

automatically, manual analysis was necessary. It takes approximately 20 minutes for a physician to manually analyze a video and to derive FCD value accordingly. Physicians provided FCD values for 129 video recordings captured from 36 patients. Only one of the physicians analyzed all 129 videos. Therefore for some of the videos, there is only one manually derived FCD value, there are 2 FCD values for some videos, for some others 3 or more FCD values are available for comparison. The presented algorithm is applied to all videos and the results of the algorithm is compared to the median and the average of manual FCD values.

The segmentation results are first evaluated. After segmenting all of the vessels that meet the diameter criteria, difference calculation part of the algorithm removes capillaries without flow from the segmentation results. An example of a microcirculation video frame that includes no-flow capillaries is shown before and after difference calculation in Figure 6.5 and Figure 6.6.

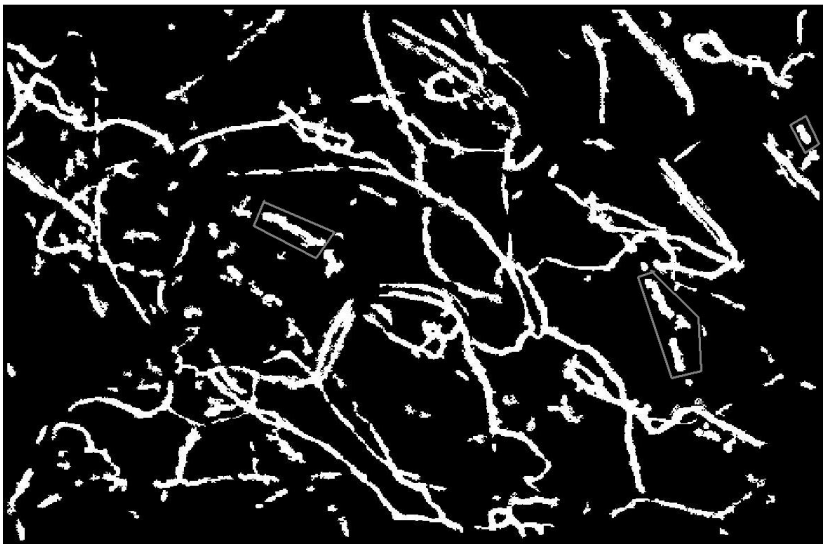

Figure 6.5: Result of segmentation algorithm with all vessels.

Figure 6.5 is the result of segmentation algorithm with all blood vessels included. The vessels without flow are surrounded with gray lines. These vessels are removed by applying the algorithm proposed in Difference Calculation section in Figure 6.6. Three sublingual microcirculation frames and the result of presented algorithm are displayed in Figure 6.7. Automatically derived FCD value is 15.17% for the first image whereas the median FCD of manual analysis is 15.86%. FCD result of the algorithm for the image in the second row is 15.16% compared to the manual FCD of 15.58%. For the third frame in Figure 6.7, FCD is calculated as 19.45% and physicians derived an FCD

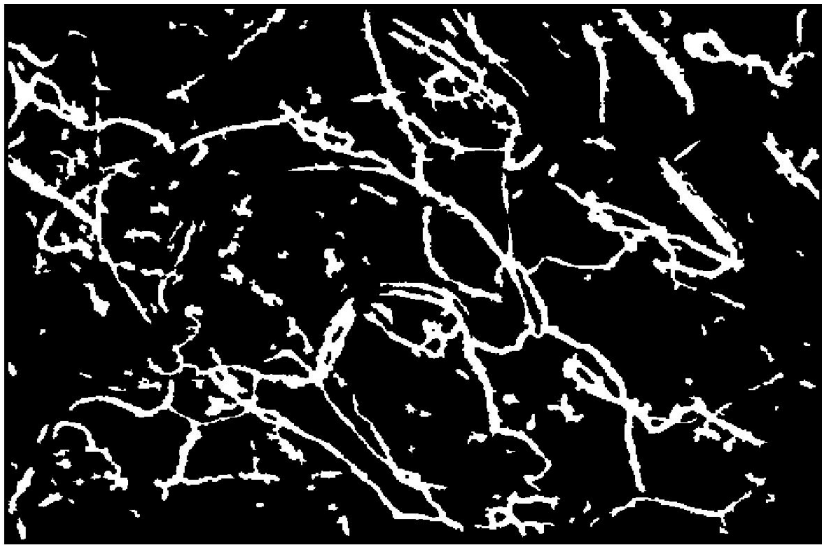

Figure 6.6: Result of difference calculation algorithm with active vessels only.

value of 20.74%.

Bland-Altman plots are provided to compare FCD results of the algorithm with manually derived FCD values. The first plot in Figure 6.8 is a comparison of results of the algorithm and the median of manual analysis. Bland-Altman plot is widely used to compare two clinical measurement methods. The x-axis in the plot is the mean value of two measurements for each data point. The y-axis is the difference between two measurements for each data point. The mid-line shows the mean value of the difference. The upper and lower lines indicate 95% interval which is calculated by the mean of difference between two measurement methods $\pm$ 1.96*standard deviation of the difference; $\mu(difference) \pm 1.96 * std(difference)$. Bland-Altman plot of presented algorithm and the mean of manual analysis is provided in Figure 6.9. Third Bland-Altman plot is the comparison between the manual analysis made by two physicians given in Figure 6.10. Since the second physician analyzed only 97 of the videos, the comparison is made based on 97 data points instead of 129.

As it can be seen, the Bland-Altman plots indicate that the variations between the analysis made by two physicians are comparable, if not more than the variations between automated system and the mean or median of the analysis of all physicians. This will be discussed further in he next chapter.

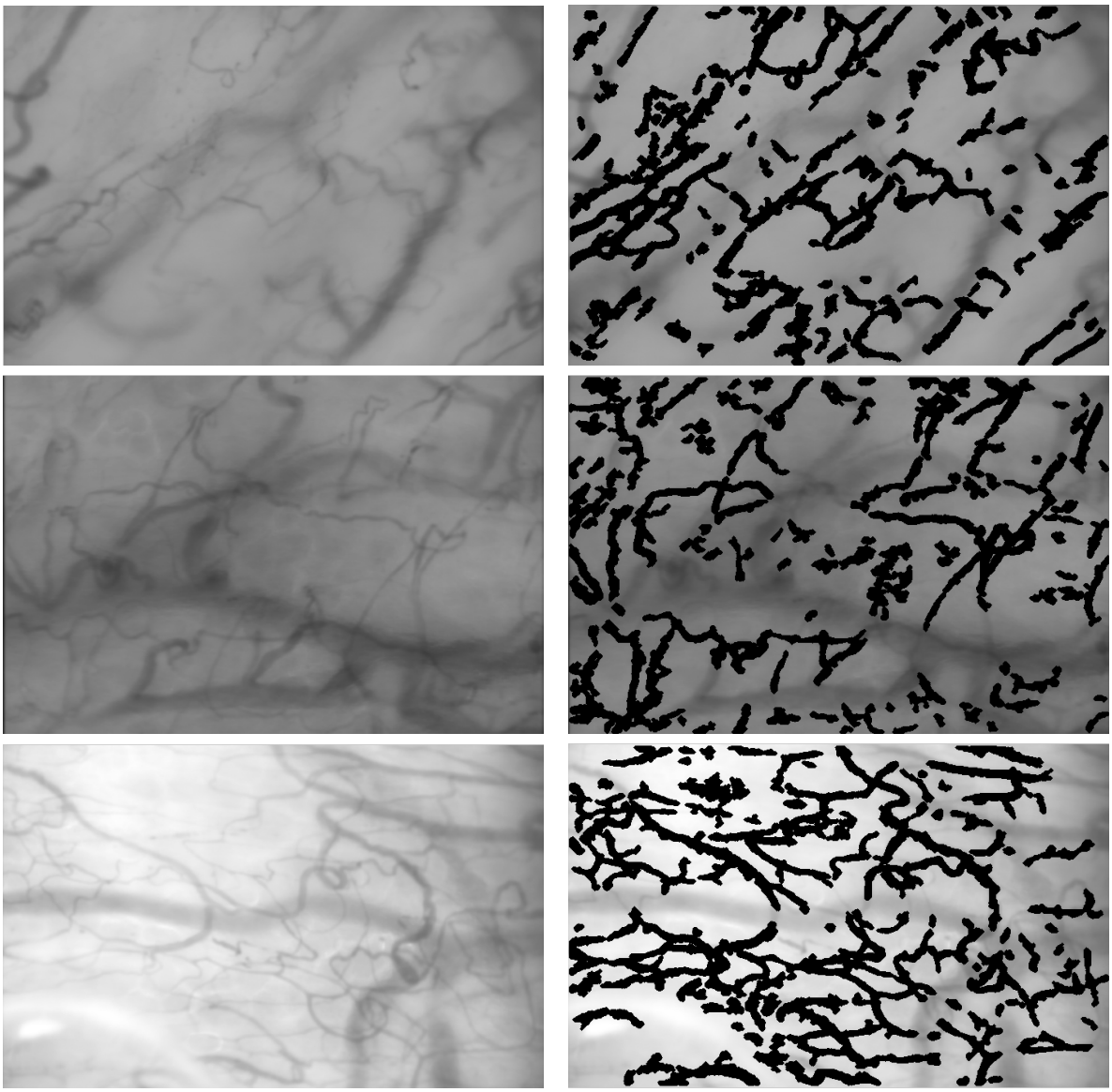

Figure 6.7: Results of the algorithm for three sublingual human microcirculatory videos, original frames on the left and segmented active capillaries on the right.

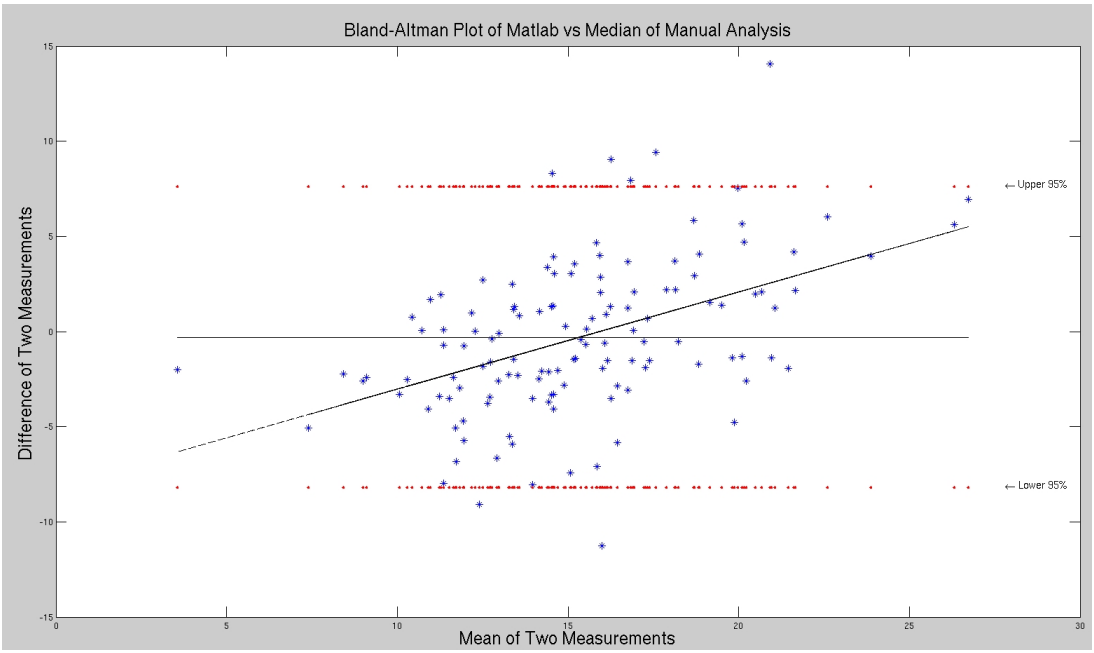

Figure 6.8: Bland-Altman plot of FCD values from the algorithm and median of manual FCD values.

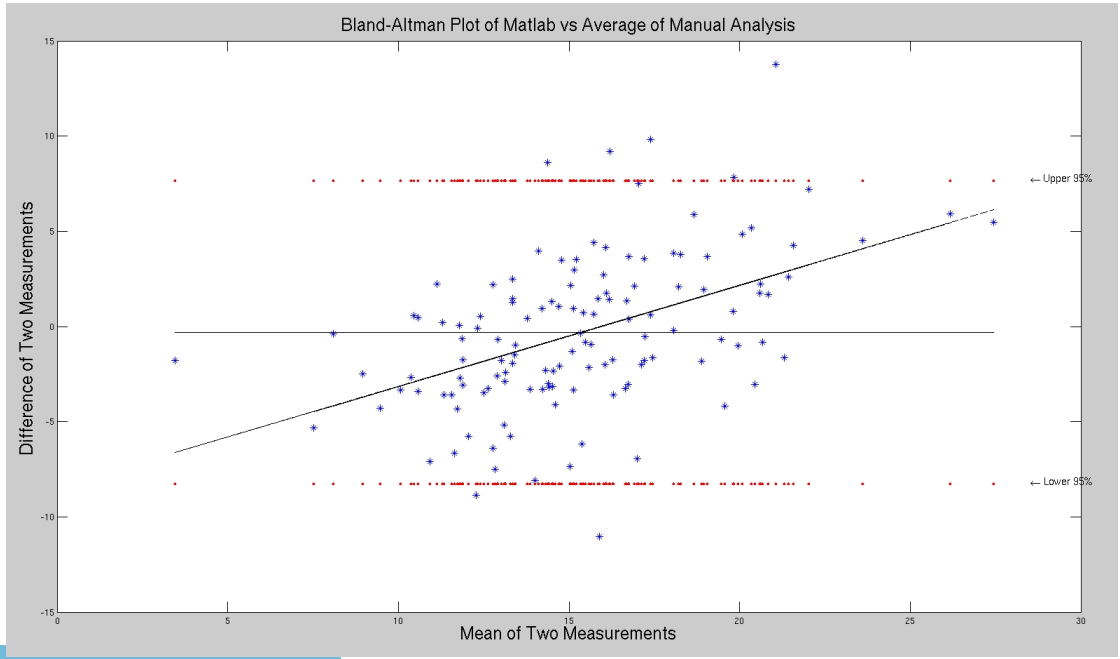

Figure 6.9: Bland-Altman plot of FCD values from the algorithm and mean of manual FCD values.

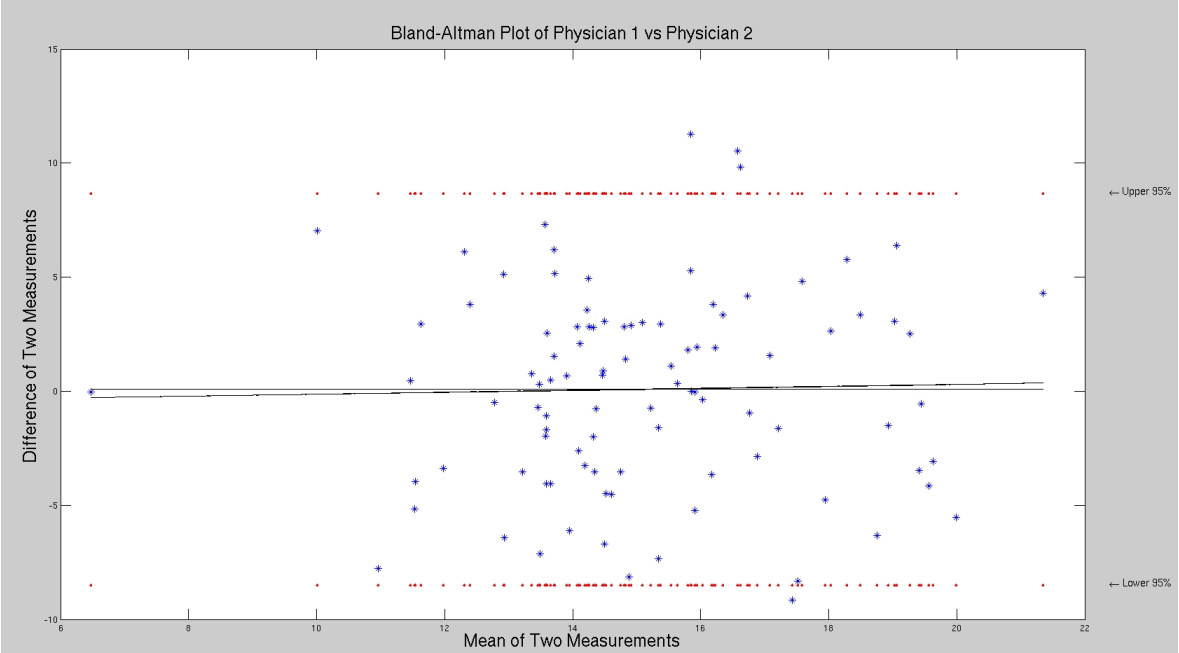

Figure 6.10: Bland-Altman plot of FCD values for two different manual analysis.

Furthermore, Bland-Altman plot of FCD values from the algorithm and from the analysis of individual physicians are also provided in Figure 6.11 and Figure 6.12.

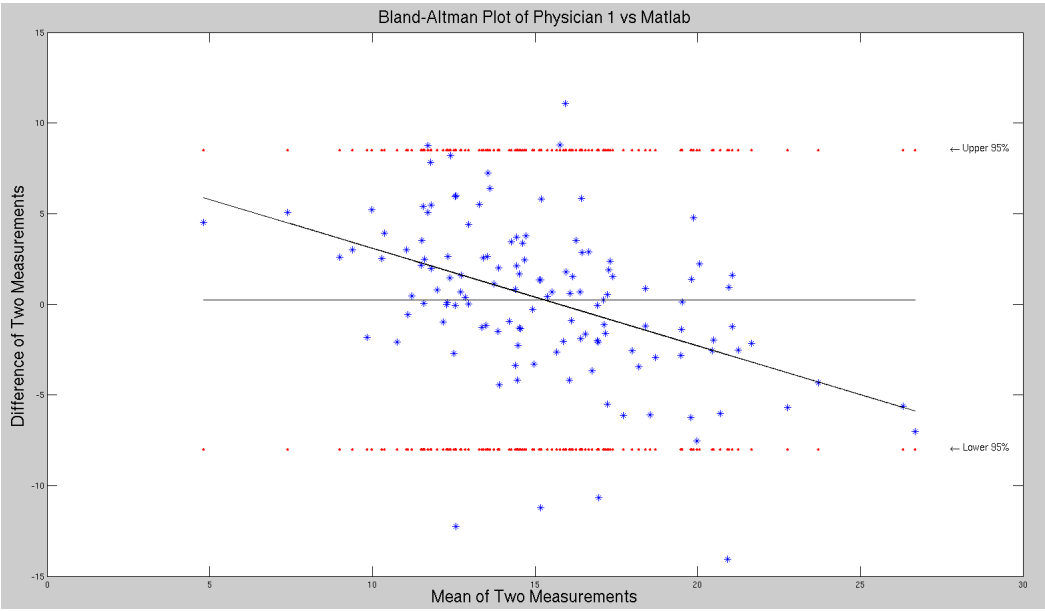

Figure 6.11: Bland-Altman plot of FCD values from the algorithm and from the analysis of physician 1.

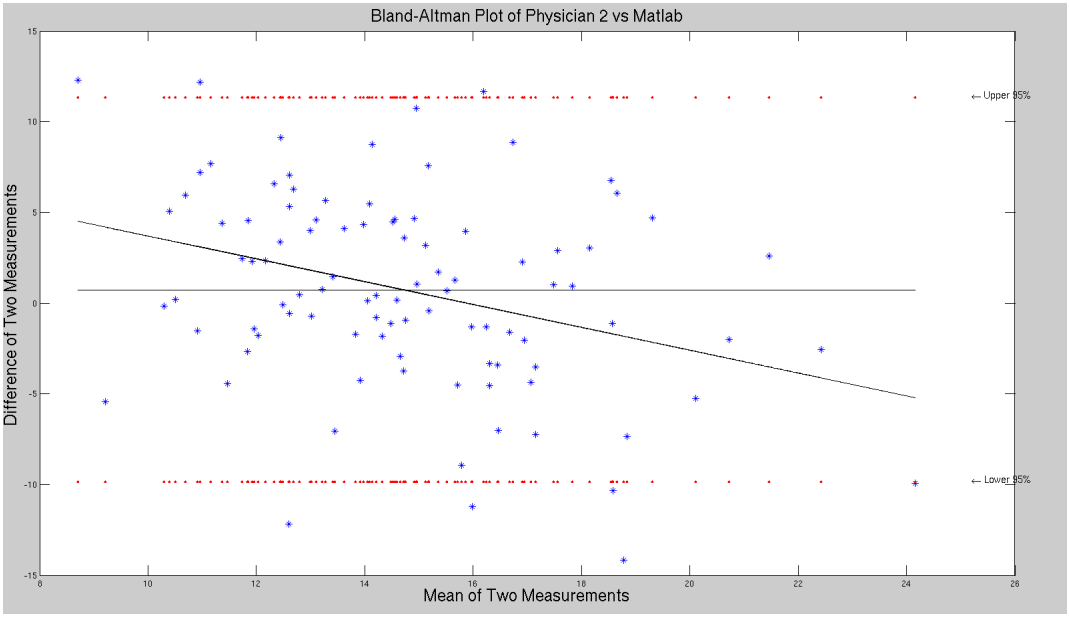

Figure 6.12: Bland-Altman plot of FCD values from the algorithm and from the analysis of physician 2.

Table 6.2 gives the FCD values for all subjects calculated as: median of manual analysis results, automatically calculated by the presented method, the difference between the median of manual analysis and MATLAB results, the mean of manual analysis and MATLAB results. In Table 6.2, the cases where the lighting on the camera was not sufficient were not included. The mean of difference between manual analysis and MATLAB results, standard deviation of the difference and 95% interval are provided in Table 6.3.

6.2 Results of Retinal Vessel Segmentation

To verify the vessel segmentation algorithm, it is tested on two publicly available retinal image databases. The images in the DRIVE database [94] are captured during a diabetic retinopathy screening program. Among photographs from 400 diabetic subjects of ages between 25-90, forty images are randomly selected. 33 subjects do not show any sign of diabetic retinopathy and 7 of them show signs of mild diabetic retinopathy. The retinal images are in RGB format, green channel of the retinal images is used for this study. Twenty of the retinal images are provided for training purpose and twenty for testing. For twenty test images, two manual segmentations of the vasculature are available whereas there is a single manual segmentation for the training set.

The images were acquired using a Canon CR5 non-mydriatic 3CCD camera with a 45 degree field of view (FOV). Each image was captured using 8 bits per color plane at 768 by 584 pixels. The FOV of each image is circular with a diameter of approximately 540 pixels. The images are compressed in JPEG format. Mask images are also provided in this database to identify FOV. An example of RGB retinal image from DRIVE is shown in Figure 6.13.

Figure 6.13: An RGB retinal image from DRIVE database.

The mask image for Figure 6.13 is depicted in Figure 6.14.

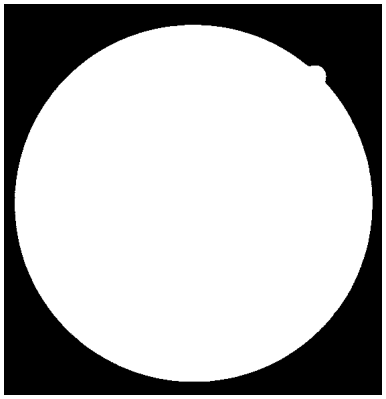

Figure 6.14: FOV of the retinal image in Figure 6.13 from DRIVE database.

The STARE database consists of 20 retinal images captured using a TopCon TRV-50 fundus camera at 35° FOV. The images are digitized to 700 by 605 pixels with 8 bits per channel. In the images, the FOV is around $650 * 550$ pixels. Ten images contain pathology. All images are manually segmented by two observers. The first observer marked 10.4% of the pixels as vessel whereas the second observer marked 14.9%.

From DRIVE database, twenty test images are segmented using the vessel segmentation method described in the related chapter and results are compared with two manually labeled images. The green channel is used for both DRIVE and STARE images. For both databases, the results of presented segmentation method are compared with the two manual segmentations. In addition, the two manual segmentation results are compared with each other.

The green channel of the original retinal images, the two manual segmentations provided by DRIVE, and the results of presented methods for three images are demonstrated in Figure 6.15.

Results of STARE database are displayed in Figure 6.16.

Results are compared with manually labeled images by calculating the Maximum Average Accuracy (MAA). The absolute difference between two segmentation results is calculated pixel by pixel for the region of interest. The summation of difference is divided by the total number of pixels in the region of interest and subtracted from 1. The equation for MAA is given as follows:

$$MAA = 1 - \sum_{i=1}^{M} \sum_{j=1}^{N} \left| \frac{MS_{i,j} - AS_{i,j}}{M.N} \right| \tag{6.1}$$

For an image of width M and height N, the manual segmentation result is labeled as 'MS' and the result of segmentation algorithm is labeled as 'AS'.

The ratio of false-positive (background pixels detected as vessel) and false-negative (vessel pixels detected as background) are also calculated. The average values of test results for DRIVE and STARE databases are displayed in Table 6.4 and Table 6.5.

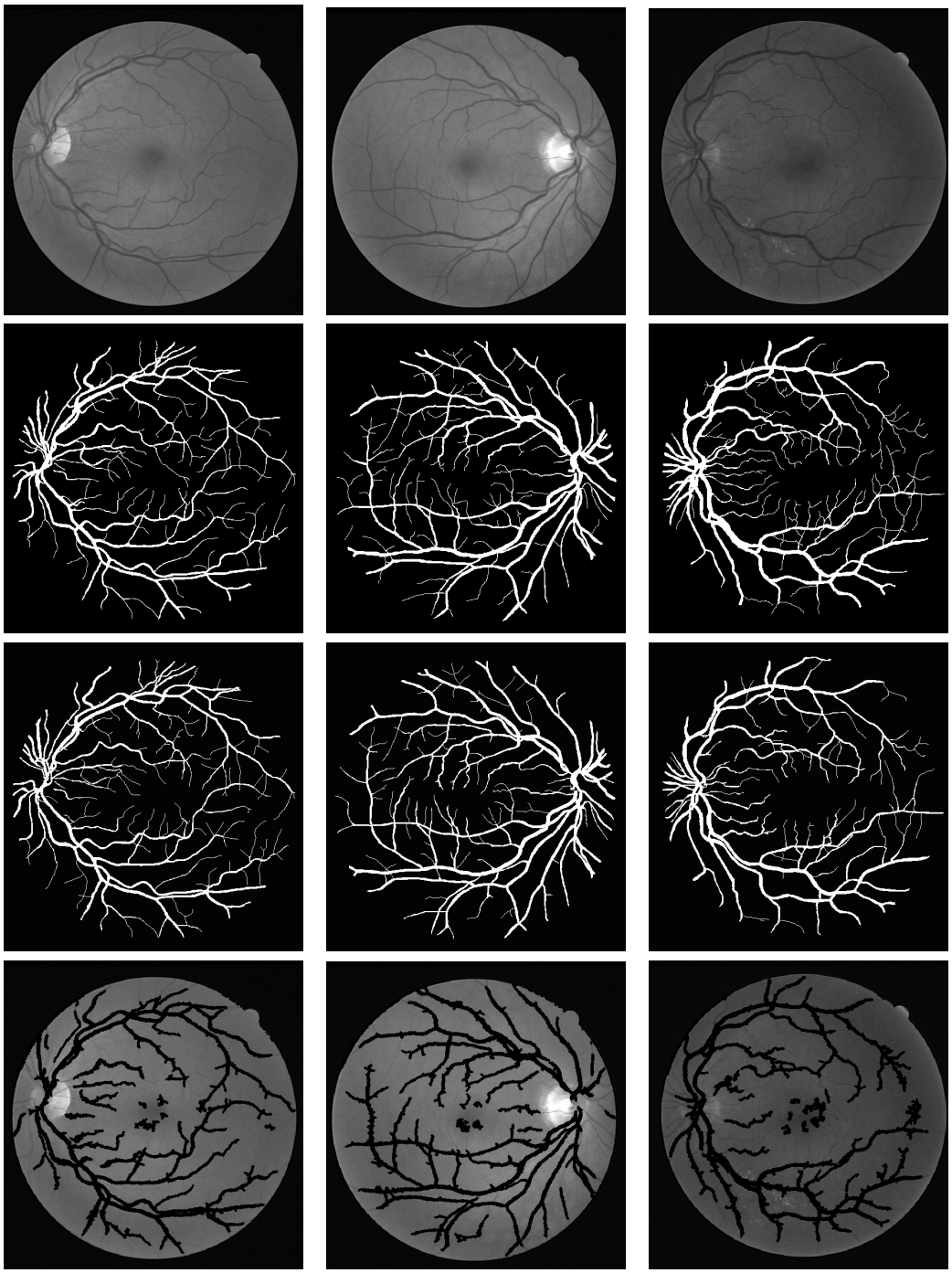

Figure 6.15: First row: Green channel of retinal images from DRIVE. Second row: First manual segmentation. Third row: Second manual segmentation. Fourth row: Results of presented method.

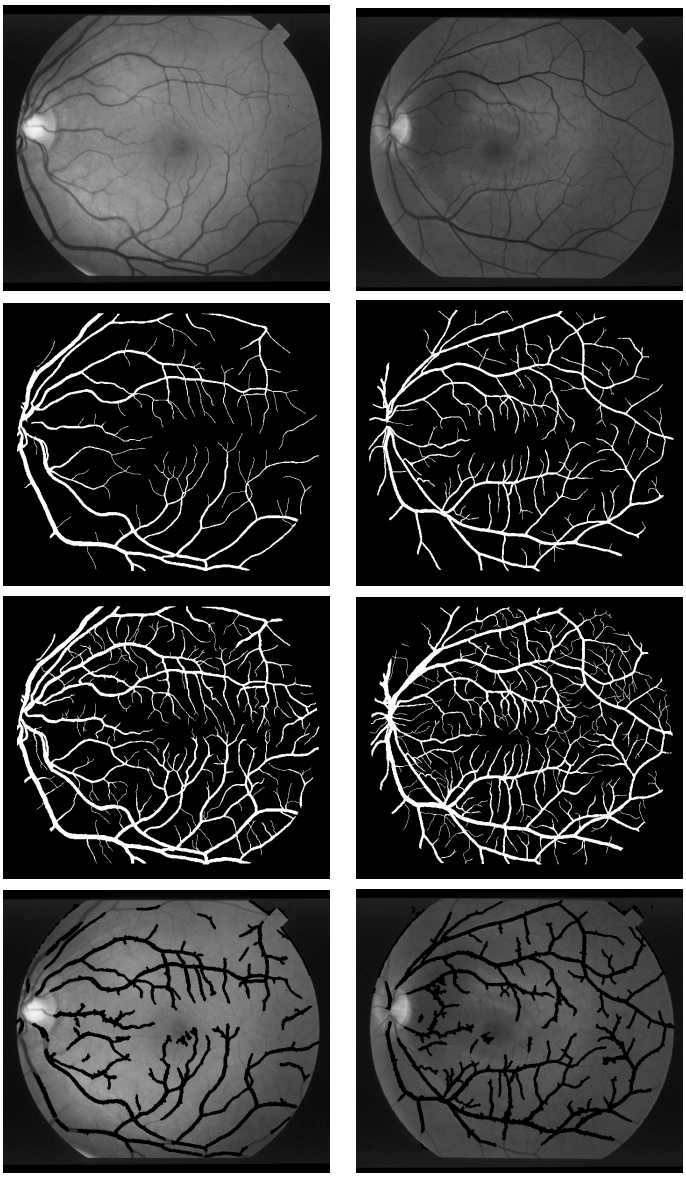

Figure 6.16: First row: Green channel of retinal images from STARE. Second row: First manual segmentation. Third row: Second manual segmentation. Fourth row: Results of presented method.

Table 6.2: FCD values for 129 subjects; median of manual analysis, automatically calculated with Matlab, and the difference, mean of 2 measurement methods(manual and Matlab)

	Manual	Matlab	Diff	Mean		Manual	Matlab	Diff	Mean
Data 1	15.860	15.178	0.682	15.519	Data 65	13.500	18.150	-4.650	15.825
Data 2	13.890	15.240	-1.350	14.565	Data 66	16.280	19.979	-3.699	18.129
Data 3	15.590	16.907	-1.317	16.248	Data 67	18.510	17.968	0.542	18.239
Data 4	20.520	19.122	1.398	19.821	Data 68	15.470	15.615	-0.145	15.542
Data 5	17.810	22.513	-4.703	20.162	Data 69	11.560	9.036	2.524	10.298
Data 6	11.690	12.677	-0.987	12.183	Data 70	14.250	11.669	2.581	12.960
Data 7	14.140	12.679	1.461	13.409	Data 71	14.430	10.994	3.436	12.712
Data 8	19.640	21.725	-2.085	20.683	Data 72	15.360	7.368	7.992	11.364
Data 9	19.520	23.710	-4.190	21.615	Data 73	13.300	9.763	3.537	11.531
Data 10	14.530	10.761	3.769	12.645	Data 74	17.650	16.120	1.530	16.885
Data 11	12.270	12.274	-0.004	12.272	Data 75	16.310	10.412	5.898	13.361
Data 12	16.960	7.862	9.099	12.411	Data 76	12.120	14.603	-2.483	13.362
Data 13	20.570	22.732	-2.162	21.651	Data 77	13.160	14.001	-0.841	13.581
Data 14	23.500	29.130	-5.630	26.315	Data 78	15.905	14.448	1.457	15.176
Data 15	13.310	10.357	2.953	11.834	Data 79	16.615	12.542	4.073	14.578
Data 16	12.840	13.995	-1.155	13.417	Data 80	18.785	11.360	7.425	15.072
Data 17	15.270	13.174	2.096	14.222	Data 81	16.975	15.051	1.924	16.013
Data 18	18.000	9.947	8.053	13.973	Data 82	16.220	12.934	3.286	14.577
Data 19	13.410	16.978	-3.568	15.194	Data 83	16.180	12.839	3.341	14.510
Data 20	15.480	13.375	2.105	14.428	Data 84	4.558	2.565	1.992	3.561
Data 21	13.570	16.624	-3.054	15.097	Data 85	15.380	16.049	-0.669	15.714
Data 22	14.240	9.164	5.076	11.702	Data 86	10.040	10.810	-0.770	10.425
Data 23	19.360	13.522	5.838	16.441	Data 87	10.310	12.250	-1.940	11.280
Data 24	17.230	20.169	-2.939	18.699	Data 88	10.320	7.901	2.420	9.110
Data 25	15.580	15.161	0.419	15.371	Data 89	13.090	16.119	-3.029	14.604
Data 26	14.920	18.575	-3.655	16.748	Data 90	10.130	11.813	-1.683	10.972
Data 27	18.020	14.497	3.523	16.259	Data 91	11.720	10.998	0.722	11.359
Data 28	18.310	15.219	3.091	16.764	Data 92	10.400	18.693	-8.293	14.547
Data 29	16.280	12.585	3.695	14.432	Data 93	10.680	10.752	-0.072	10.716
Data 30	16.130	17.362	-1.232	16.746	Data 94	14.820	9.073	5.747	11.947
Data 31	17.050	19.253	-2.203	18.152	Data 95	9.546	7.320	2.226	8.433
Data 32	13.020	12.940	0.080	12.980	Data 96	13.530	11.941	1.590	12.735
Data 33	9.930	4.861	5.070	7.395	Data 97	14.280	9.569	4.711	11.924
Data 34	12.960	12.573	0.387	12.767	Data 98	12.940	8.863	4.077	10.902
Data 35	15.720	13.681	2.040	14.700	Data 99	13.420	11.600	1.820	12.510
Data 36	16.040	10.520	5.521	13.280	Data 100	15.720	12.213	3.507	13.967
Data 37	15.920	14.500	1.420	15.210	Data 101	16.300	13.463	2.837	14.881
Data 38	19.680	17.966	1.714	18.823	Data 102	13.860	15.159	-1.299	14.510
Data 39	15.900	17.978	-2.078	16.939	Data 103	14.690	12.380	2.310	13.535
Data 40	18.170	16.626	1.544	17.398	Data 104	16.820	20.893	-4.073	18.857
Data 41	12.840	10.439	2.401	11.640	Data 105	13.950	17.937	-3.987	15.943
Data 42	11.310	11.387	-0.077	11.349	Data 106	23.260	30.197	-6.937	26.729
Data 43	15.670	16.586	-0.916	16.128	Data 107	14.530	17.368	-2.838	15.949
Data 44	21.650	20.258	1.392	20.954	Data 108	18.400	19.913	-1.513	19.156
Data 45	16.210	23.753	-7.543	19.982	Data 109	16.780	18.982	-2.202	17.881
Data 46	10.290	7.705	2.585	8.997	Data 110	19.580	25.614	-6.034	22.597
Data 47	12.330	11.558	0.772	11.944	Data 111	11.720	8.405	3.315	10.062
Data 48	17.490	16.957	0.534	17.223	Data 112	20.740	19.446	1.294	20.093
Data 49	15.770	21.600	-5.830	18.685	Data 113	15.150	8.308	6.842	11.729
Data 50	16.910	15.392	1.518	16.151	Data 114	20.430	21.683	-1.253	21.056
Data 51	14.950	16.979	-2.029	15.964	Data 115	18.820	20.205	-1.385	19.512
Data 52	15.390	12.889	2.502	14.139	Data 116	12.780	14.081	-1.301	13.430
Data 53	16.400	15.775	0.625	16.087	Data 117	13.900	27.945	-14.045	20.922
Data 54	22.250	17.478	4.772	19.864	Data 118	12.870	20.794	-7.924	16.832
Data 55	17.860	15.022	2.838	16.441	Data 119	19.490	21.468	-1.978	20.479
Data 56	11.740	20.789	-9.049	16.265	Data 120	22.410	20.484	1.926	21.447
Data 57	21.530	18.927	2.603	20.229	Data 121	17.270	22.927	-5.657	20.098
Data 58	21.890	25.867	-3.977	23.878	Data 122	14.790	15.058	-0.268	14.924
Data 59	16.240	9.576	6.664	12.908	Data 123	12.610	16.535	-3.925	14.572
Data 60	12.940	9.546	3.394	11.243	Data 124	12.720	16.086	-3.366	14.403
Data 61	13.650	14.685	-1.035	14.167	Data 125	14.400	12.116	2.284	13.258
Data 62	21.620	10.379	11.241	15.999	Data 126	16.990	17.684	-0.694	17.337
Data 63	19.410	12.297	7.113	15.854	Data 127	18.220	16.310	1.910	17.265
Data 64	11.150	13.872	-2.722	12.511	Data 128	16.890	16.939	-0.049	16.914
					Data 129	12.870	22.289	-9.419	17.580

Table 6.3: Mean of difference between manual analysis and Matlab, standard deviation of the difference and 95% interval values

Mean Diff	STD Dif	Up 95%	Low 95%
0.3036	4.0321	8.206	-7.599

Table 6.4: Comparison of Segmentation with Manually Segmented Retinal Images for DRIVE.

	MAA	***False Positive Rate*** %	***False Negative Rate*** %
Presented wrt 1^{st} observer	0.9216	1.95	5.89
Presented wrt 2^{nd} Observer	0.9270	1.91	5.39
1^{st} Observer wrt 2^{nd} Observer	0.9472	2.40	2.88

Table 6.5: Comparison of Segmentation with Manually Segmented Retinal Images for STARE.

	MAA	***False Positive Rate*** %	***False Negative Rate*** %
Presented wrt 1^{st} observer	0.9324	1.47	5.29
Presented wrt 2^{nd} Observer	0.8998	0.94	9.08
1^{st} Observer wrt 2^{nd} Observer	0.9367	5.33	1.00

Chapter 7

Discussion of Results and Conclusion

7.1 Discussion

The algorithm is implemented on a Pentium 4, CPU 3.20 GHz computer. MATLAB R2009a is the computer software used to code the algorithm. Computational time required for an 80 frame video is around 20 minutes. This time is reduced by implementing the algorithm in C++ from 20 minutes to about 1 minute.

- The segmentation algorithm applied to microcirculatory images seems to be capable of segmenting all blood vessels in the defined geometrical range. Since the main goal is microcirculation assessment, wide vessels are excluded automatically by defining P_d parameter.
- The contribution of three parameters, diameter, angle and contrast ratio, is analyzed by leaving out one parameter at a time and running the segmentation algorithm with other two parameters. The results are presented in Figure 7.1. In Figure 7.1(a), pixels are verified based on two measurements; angle and contrast ratio. When it is compared to Figure 7.1(d), the wide vessels that do not belong to microcirculation are segmented in Figure 7.1(a). Without the use of angle parameter, as it is seen in Figure 7.1(b), large clouds of background are segmented as vessels. As it is expected, leaving out the contrast ratio results more background pixels to be segmented as vessel, Figure 7.1(c). As a result, using all three parameters; diameter, angle and contrast ratio results in an accurate segmentation in Figure 7.1(d).
- Segmentation algorithm was successful in healthy as well as diseased, in this case hemorrhagic, subjects. As it is shown in Figure 6.3, the quality of video recordings from hemorrhagic

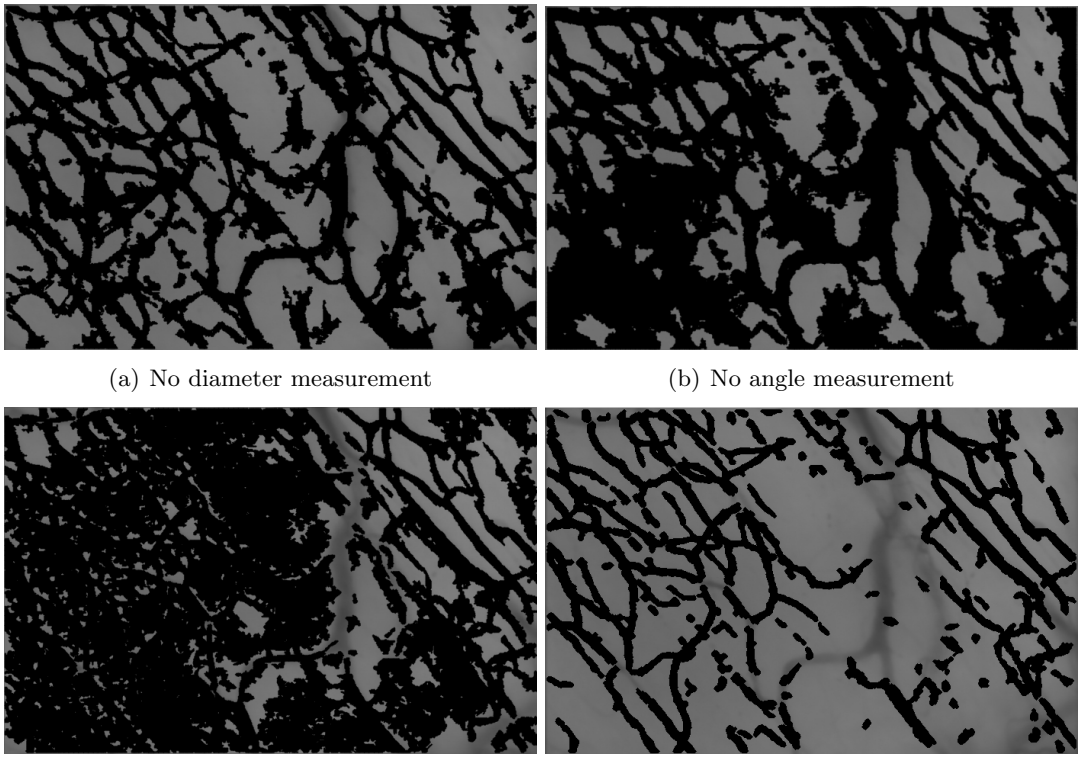

(a) No diameter measurement (b) No angle measurement

(c) No contrast ratio measurement (d) Using all three measurements

Figure 7.1: Results of segmentation using two parameters only and Figure 7.1(d) is the result using all three parameters.

subjects is very low due to limited blood flow. Nevertheless the algorithm is successful in segmenting a few vessels with RBCs in such video recordings.

- An adaptive strategy is generated to select local P_c values which is described in Chapter 5. This is perhaps the most important characteristic of the algorithm, as without this local adjustments in P_c, poor segmentations were achieved. Examples of the varying contrast ratio across different frames and across the same frame are displayed in Figure 4.13. Selecting local P_c values adaptively results acceptible segmented images regardless of darker and/or brighter areas in these images. Without local computation of P_c value, the segmentation results of the algorithm with global P_c for images in Figure 4.13 are presented in Figure 7.2 and Figure 7.4. Results of the algorithm with local P_c values are demonstrated in Figure 7.3 and Figure 7.5.

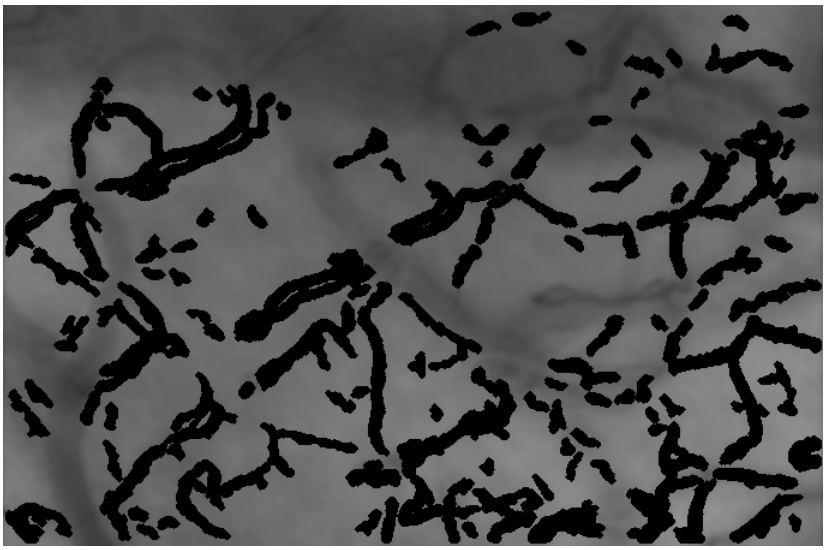

Figure 7.2: Segmented active capillaries for the image in Figure 4.13(a) by applying a global P_c.

As mentioned before, the adjustments in the value of P_c are made through a rule-set formed using machine learning algorithms that consider local statistical properties of each region.

- One of the issues faced during vessel segmentation process is the overlapping blood vessels. In some of the videos, a wide and dark vessel is underlying beneath thin capillaries. An example frame is shown in Figure 7.6. Since the diameter parameter is rejecting the wide vessels, the thinner vessel pixels overlapping the wide vessels are rejected. The result of segmentation

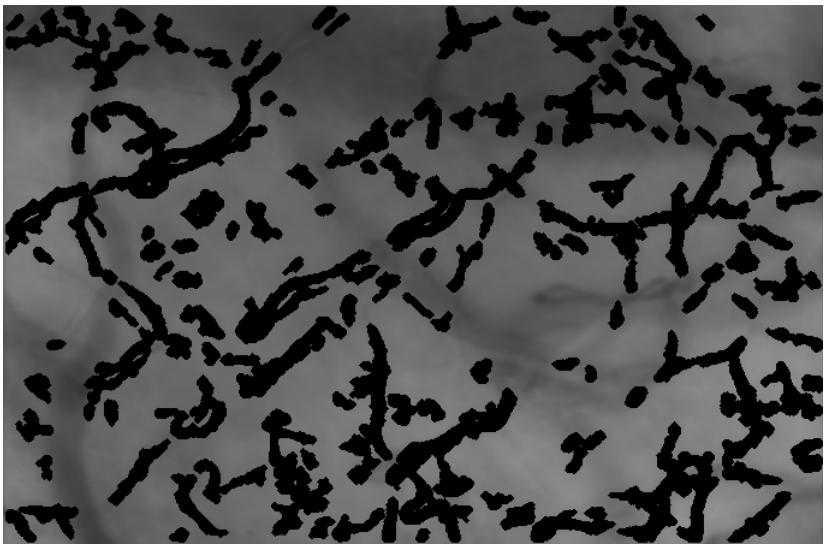

Figure 7.3: Segmented active capillaries for the image in Figure 4.13(a) by applying local P_c.

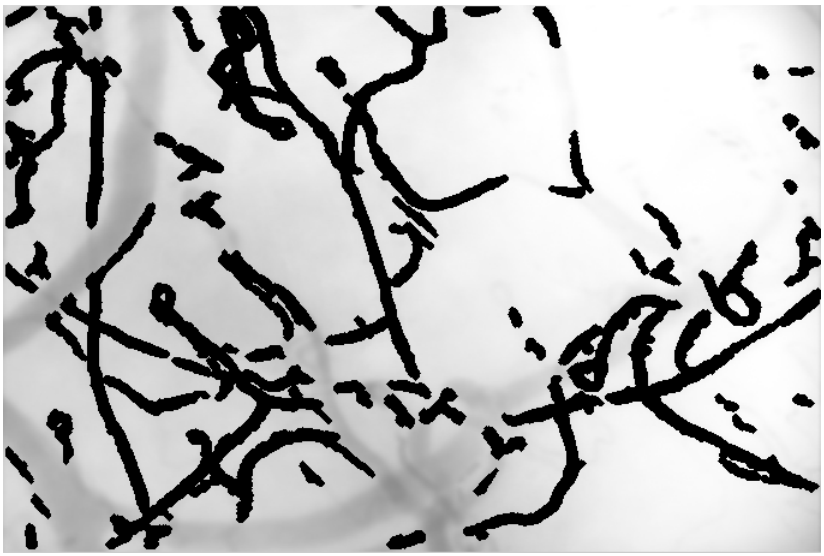

Figure 7.4: Segmented active capillaries for the image in Figure 4.13(b) by applying a global P_c.

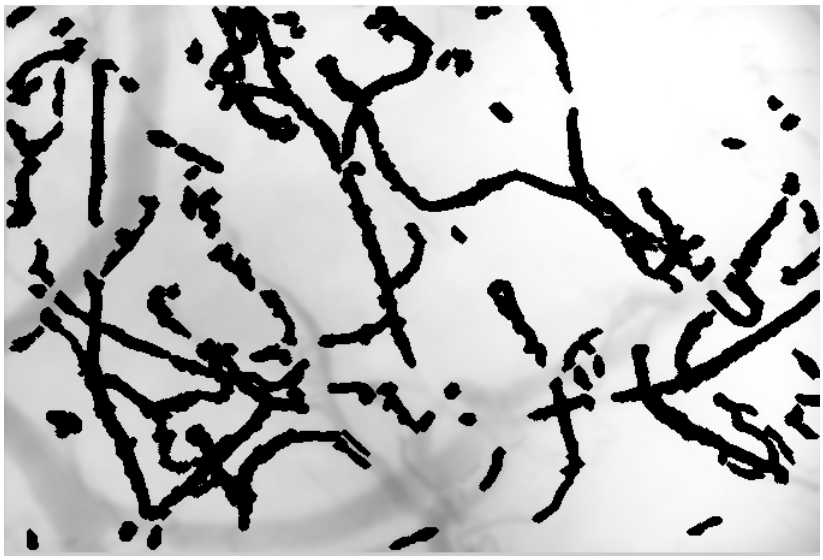

Figure 7.5: Segmented active capillaries for the image in Figure 4.13(b) by applying local P_c.

for Figure 7.6 is depicted in Figure 7.7. The thinner vessels are extracted where there is no overlapping but segmentation fails on those overlapping regions. This condition causes under-segmentation and gives a lower FCD value with respect to the manual analysis.

- The quality of sublingual microcirculation video recordings are affected in the presence of saliva. In particular, a large amount of bubbles in some of the videos interferes with the segmentation algorithm results in over segmented images and higher FCD values than expected FCD. Figure 7.8 presents a problematic frame due to presence of bubbles.

- Video recordings were successfully stabilized using proposed stabilization algorithm. The RMS error value indicates the significant reduction with a p-value of less than 0.0001. The accuracy of labeling frames as 'in transition' is visually verified.

- The stabilization algorithm is based on linear transformation of microcirculation frames. The amount of displacement is calculated by averaging the displacement in x and y directions. In 5 of 129 videos, a non-linear translation is recorded according to the movement of the tongue. Since non-linear transformation is not a common case in the currently available dataset, the presented stabilization algorithm was capable of eliminating undesired motion from the microcirculatory video recordings.

- The algorithm segmented vessel network of retinal images with an accuracy of 92% for DRIVE

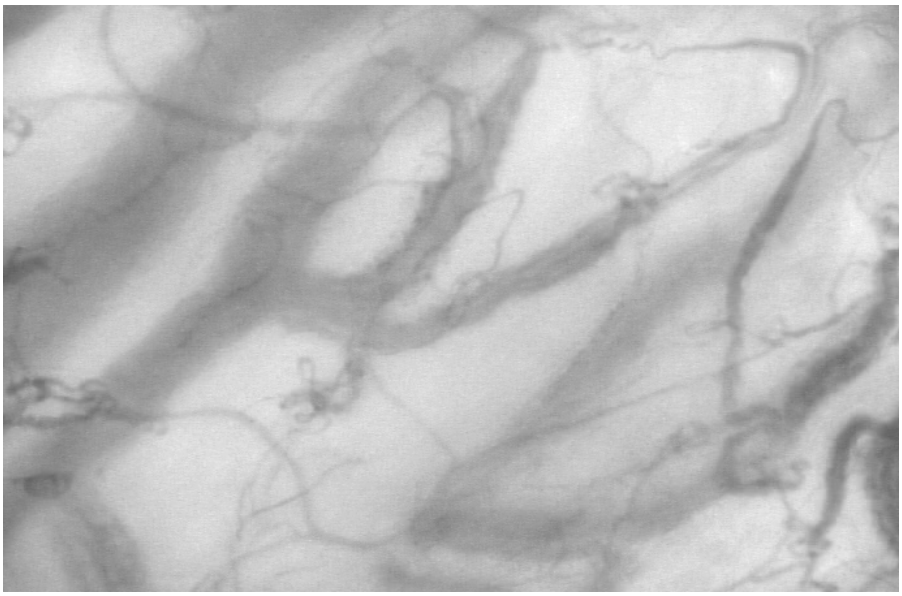

Figure 7.6: A microcirculatory image with overlapping vessels.

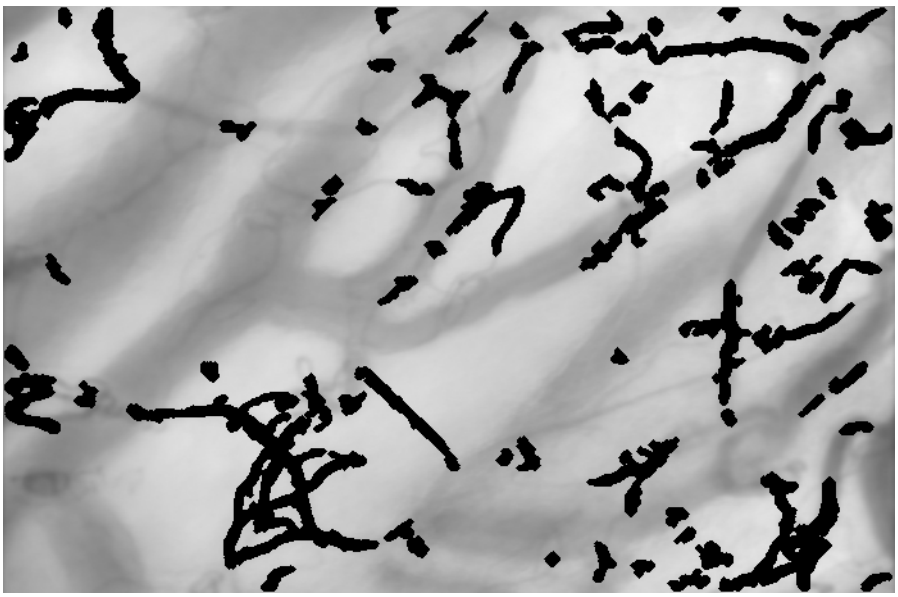

Figure 7.7: Thinner vessels are not segmented in overlapping regions.

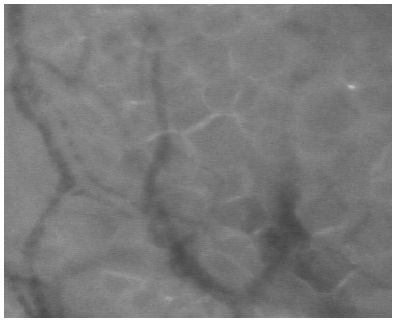

Figure 7.8: Bubbles interfering with segmentation of sublingual microcirculatory images.

database and an accuracy of 93% for STARE database. According to the MAA values , the accuracy of the algorithm is comparable to the algorithm proposed by Jiang et al. [105], which is considered as one the most successful unsupervised method developed for retinal image segmentation. Even though the propsoed methodology is not designed for retinal images, the performance seems to be at least as desirable as Jiang's (with MAA 0.92 and 0.93). However the performance needs to be improved to decrease false-negative-rate as it is shown in Table 6.4. Note that, the same rule-set, generated to select local P_c, trained with windows from microcirculation videos, is applied to retinal images. A local P_c rule-set that is generated with retinal images is expected to result to much higher accuracy in retinal vessel segmentation.

- Calculated FCD values presented in Table 6.1 can be used to identify hemorrhagic subjects from healthy subjects. A threshold FCD value of approximately 12% seems to be a cut-off value to seperate these two groups. However, the algorithm needs to be tested on more subjects.

- Automatically calculated FCD values are compared with FCD values derived by multiple physicians and the results of the algorithm are proved to be consistent with the manual analysis. Even though the variance between the manual analysis and that of the presented method seems to be slightly high in Figure 6.8 and Figure 6.9, it is not higher than the variance across the two manual analysis as shown in Figure 6.10.

7.2 Conclusion

- A new method was introduced to automatically analyze microcirculation video recordings, compute quantitative parameters and form the basis for diagnostic decisions for a number of injuries and illnesses. Presented algorithm is capable of stabilizing microcirculatory video recordings, segmenting all the blood vessels and capillaries with specified geometric structures, identifying the vessels with blood flow and calculating FCD parameters automatically for healthy and non-healthy subjects.

- The vessel segmentation algorithm was applied to microcirculatory videos as well as two publicly available retinal image databases (DRIVE and STARE). The results are shown to be highly accurate for both data types even though system is designed for microcirculatory videos. Therefore, one can conclude that the presented vessel segmentation algorithm is not case-based, it can easily be applied to other medical images with small modifications.

- The predicted FCD values, when compared with physicians' derivations show high level accuracy and reliability. Bland-Altman plots show that results were consistent with manually derived FCD values. The results of the algorithm fall into the 95% interval of manual analysis results. Presented system has a high potential in decreasing decision making time and allowing more accurate diagnosis.

- Currently available microcirculation analysis software packages lack automation, accuracy or stabilization. Proposed system addresses these issues using a novel approach. Close-to-real-time, automated and quantitative analysis of microcirculation will facilitate routine clinical use.

- Although the analysis was done on lingual and/or sublingual images captured by Microscan SDF imaging system, the method is applicable on other microcirculation images. Cytoscan Video Microscope is a commercially available instrument that produces high-contrast microvascular images during surgery, research and clinical diagnostic applications. The resulting computational tool is applicable in anesthesiology, orthopedic surgery, cardiac surgery, critical care, gastrointestinal imaging, gynecology, laparoscopic and endoscopic images, and neurosurgery and transplant surgery imaging.

Chapter 8

Future Work

The continuation of the presented research will target the following objectives:

1. Blood Flow Scoring: In the presented research, vessels are categorized in two groups according to the blood flow: with flow and without flow. Some clinicians and researchers prefer to score Microcirculatory Flow Index (MFI) in four groups (0=no flow, 1=intermittent, 2=sluggish, 3=normal) [11]. In future, the difference calculation method can be customized to provide users MFI scoring in four groups.

2. Velocity: The velocity of blood flow in microcirculatory videos is not calculated in this research. Automated and accurate computation of velocity may result to a useful flow velocity measure to be used for quantitative analysis of microcirculation.

3. Dataset: The dataset used for this research only includes hemorrhagic swine subjects and human patients with heart failure problems. To correlate between microcirculation parameters and different illnesses and injuries, a larger dataset will be created.

4. Microcirculation Parameters: In this research, FCD and MFI are the only calculated parameters to measure microcirculation. Further studies will include other scores of microcirculation for a detailed analysis, such as proportion of perfused vessels (PPV). PPV is calculated as follows:

$$PPV = 100 * \frac{\text{total number of blood vessels} - [\text{no flow} + \text{intermittent flow}]}{\text{total number of vessels}} \tag{8.1}$$

Bibliography

[1] W. Groner, J. W. Winkelman, A. G. Harris, C. Ince, G. J. Bouma, K. Messmer, and R. G. Nadeau. Orthogonal polarization spectral imaging: a new method for study of the microcirculation. *Natmed*, 5:1209–1212, 1999.

[2] Z. Turek, V. Cěrný, and R. Pařízková. Noninvasive in vivo assessment of the skeletal muscle and small intestine serous surface microcirculation in rat: Sidestream dark-field (sdf) imaging. *Physiol. Res.*, 57:365–371, 2008.

[3] RF Tuma, WN Duran, and K Ley. *Handbook of Physiology Microcirculation*. Elsevier Science, 2008.

[4] AR Pries, D Neuhaus, and P Gaehtgens. Blood viscosity in tube flow: dependence on diameter and hematocrit. *Am J Physiol Heart Circ Physiol*, 263:H1770–H1778, 1992.

[5] A Krogh. *Anatomy and physiology of capillaries*. New Haven Connecticut: Yale University Press, 1929.

[6] A Krogh. Supply of oxygen to the tissues and the regulation of the capillary circulation. *J physiol (Lond)*, 52:457–474, 1919.

[7] AG Tsai, PC Johnson, and M Intaglietta. Oxygen gradients in the microcirculation. *Physiol Rev*, 83:933–963, 2003.

[8] CC Michel and EE Curry. Microvascular permeability. *Physiol Rev*, 79:703–761, 1999.

[9] U Yuan, WM Chilian, HJ Granger, and DC Zaeija. Flow modulates coronary venular permeability by a nitric oxide-related mechanism. *Am J Physiol*, 263:H641–H646, 1992.

[10] Z. A. Awan, T. Wester, and K. Kvernebo. Human microvascular imaging: a review of skin and tongue videomicroscopy techniques and analysing variables. *Clin Physiol Funct Imaging*, 30, 2010.

[11] D. De Backer, S. Hollenberg, C. Boerma, P. Goedhart, G. Büchele, G. Ospina-Tascon, I. Dobbe, and C. Ince. How to evaluate the microcirculation: report of a round table conference. *Crit Care*, 11(5):R101, 2007.

[12] RM Bateman, MD Sharpe, and CG Ellis. Bench-to-bedside review: microvascular dysfunction in sepsis: hemodynamics, oxygen transport and nitric oxide. *Crit Care Med*, 7:359–373, 2003.

[13] RP Hebbel, R Osarogiagbon, and D Kaul. The endothelial biology of sickle cell disease; inflammation and chronic vasculopathy. *Microcirculation*, 11:129–151, 2004.

[14] MJ Stuart and RL Nagel. Sickle cell disease. *The Lancent*, 364:1343–1360, 2004.

[15] BI Levy, G Ambrosio, AR Pries, and HA Struijker-Boudier. Microcirculation in hypertension: a new target for treatment? *Circulation*, 104:735–740, 2001.

[16] C Verdant and D De Backer. Monitoring of the microcirculation may help us at the bedside. *Curr Opin Crit Care*, 11(3):240–244, 2005.

[17] KA Nath, ZS Katusic, and MT Gladwin. The perfusion paradox and instability in sickle cell disease. *Microcirculation*, 11:179–193, 2004.

[18] DK Kaul and ME Farby. In vivo studies of sickle red blood cells. *Microcirculation*, 11:153–156, 2004.

[19] RM Touyz. Intracellular mechanisms involved in vascular remodeling of resistance arteries in hypertension: Role of angiotensin ii. *Experimental Physiology*, 90:449–455, 2005.

[20] EH. Serne, RO. Gans, JC. ter Maaten, GJ. Tangelder, AJ. Donker, and CD. Stehouwer. Impaired skin capillary recruitment in essential hypertension is caused by both functional and structural capillary rarefaction. *Hypertension*, 38:238–242, 2001.

[21] MA. Creager, TF. Luscher, F. Cosentino, and JA. Bechkman. Diabetes and vascular disease: pathophysiology, clinical consequences, and medical therapy: part i. *Circulation*, 108:1527–1532, 2003.

[22] O. Genzel-Boroviczeny, J. Strotgen, A. G. Harris, K. Messmer, and F. Christ. Orthogonal polarization spectral imaging (ops): A novel method to measure the microcirculation in term and preterm infants transcutaneously. *Pediatr Res*, 51:386–391, 2002.

[23] LB. Becker, ML. Weisfeldt, MH. Weil, T. Budinger, J. Carrico, K. Kern, G. Nichol, I. Shechter, R. Traystman, C. Webb, H. Wiedemann, R. Wise, and G. Sopko. The pulse initiative: scientific priorities and strategic planning for resuscitation research and life saving therapies. *Circulation*, 105(21):1562–2570, 2002.

[24] CJ. Carrico, JB. Holcomb, and IH. Chaudry. Scientific priorities and strategic planning for resuscitation research and life saving therapy following traumatic injury: report of the pulse trauma work group. post resuscitative and initial utility of life saving efforts. *Shock*, 17:165–168, 2002.

[25] Max Harry Weil, Lance Becker, Budinger Thomas, Karl Kern, Graham Nichol, Ishaiahu Shechter, Richard Traystman, Herbert Wiedemann, Robert Wise, Myron Weisfeldt, and George Sopko. Post resuscitative and initial utility in life saving efforts (pulse): A workshop executive summary. *Resuscitation*, 50, 2001.

[26] K. H. Stadlbauer, V. Wenzel, A. C. Krismer, W. G. Voelckel, and K. H. Lindner. Vasopressin during uncontrolled hemorrhagic shock: Less bleeding below the diaphragm, more perfusion above. *Anesthesia & Analgesia*, 101, 2005.

[27] CJ Murray and AD Lopez. Alternative projections of mortality and disability by cause 1990-2020: Global burden of disease study. *Lancet*, 349:1498–504, 1997.

[28] CD Deakin and IR Hicks. Ab or abc: pre-hospital fluid management in major trauma. *J Accid Emerg Med*, 11:154–157, 1994.

[29] Y. Sakr, MJ. Dubois, D. De Backer, J. Creteur, and JL. Vincent. Persistent microcirculatory alterations are associated with organ failure and death in patients with septic shock. *Critical Care Medicine*, 32(9):1825–1831, 2004.

[30] PE. Spronk, C. Ince, MJ. Gardien, KR. Mathura, HM. Oudemans van Straaten, and DF. Zandstra. Nitroglycerin in septic shock after intravascular volume resuscitation. *Lancet*, 360:1395–1396, 2002.

[31] M. Fries, M. H. Weil, Y. Chang, C. Castillo, and W. Tang. Microcirculation during cardiac arrest and resuscitation. *Critical Care Medicine*, 34:454–457, 2006.

[32] Michael N. Cocchi, Edward Kimlin, Mark Walsh, and Michael W. Donnino. Identification and resuscitation of the trauma patient in shock. *Emergency Medicine Clinics of North America*, 25, 2007.

[33] J. A. Alten, A. Moran, A. I. Tsimelzon, M. A. Mastrangelo, S. G. Hilsenbeck, V. Poli, and D. J. Tweardy. Prevention of hypovolemic circulatory collapse by il-6 activated stat3. *PLoS ONE*, 3, 2008.

[34] Daniel De Backer and Marc-Jacques Dubois. Assessment of the microcirculatory flow in patients in the intensive care unit. *Current Opinion in Critical Care*, 7:200–203, 2001.

[35] C. Heuter. Die cheilo angioskopie, eine neue untersuchungsmethode zu physiologischen. *ZBL Med Wiss*, 17:225230, 1879.

[36] O. Müller. *Die feinsten blutgefaessen des menschen.* Stuttgart E. Enke Verlag, 1939.

[37] S Freedlander and C Lenhart. Clinical observations on the capillary circulation. *Arch Intern Med*, 29:1213, 1922.

[38] JE Tooke, PE Lins, J Ostergren, U Adamson, and B Fagrell. The effects of intravenous insulin infusion on skin microcirculatory flow in type 1 diabetes. *Int J Microcirc Clin Exp*, 4:6983, 1985.

[39] D. W. Slaaf, G. J. Tangelder, R. S. Reneman, K. Jager, and A. Bollinger. A versatile incident illuminator for intravital microscopy. *Int J Microcirc Clin Exp*, 6:391–397, 1987.

[40] S Hern and PS Mortimer. Visualization of dermal blood vessels capillaroscopy. *Clin Exp Dermatol*, 24:473478, 1999.

[41] A Bollinger, K Jager, F Sgier, and J Seglias. Fluorescence microlymphography. *Circulation*, 64:11951200, 1981.

[42] A Bollinger, J Frey, K Jager, J Furrer, J Seglias, and W Siegenthaler. Patterns of diffusion through skin capillaries in patients with long-term diabetes. *N Engl J Med*, 307:13051310, 1982.

[43] R Bonner and R Nossal R. Model for laser doppler measurements of blood flow in tissue. *Appl Opt*, 20:20972107, 1980.

[44] M Hahn, C Hahn, K Brauer, and M Junger M. Skin thermoregulation during local cooling in healthy volunteers and patients with systemic sclerosis synchronous assessment of capillary red blood cell velocity, laser doppler flux and skin temperature. *Vasa*, 27:39, 1998.

[45] HN Mayrovitz and JA Leedham. Laser-doppler imaging of forearm skin: Perfusion features and dependence of the biological zero on heatinduced hyperemia. *Microvasc Res*, 62:7478, 2001.

[46] E. Chaigneau, M. Oheim, E. Audinat, and S. Charpak. Two photon imaging of capillary blood flow in olfactory bulb glomeruli. *Proc Natl Acad Sci, USA*, 100:13081–13087, 2003.

[47] V. Cěrný, Z. Turek, and R. Pařízková. Orthogonal polarization spectral imaging: a review. *Physiol. Res.*, 56, 2007.

[48] C. Ince. Sidestream dark field imaging: an improved technique to observe sublingual microcirculation. *Critical Care*, 9:72, 2005.

[49] C. Ince. The microcirculation is the motor of sepsis. *Critical Care*, 9(sppl 4):S13–S19, 2005.

[50] P. T. Goedhart, M. Khalilzada, R. Bezemer, J. Merza, and C. Ince. Sidestream dark field (sdf) imaging: a novel stroboscopic led ring-based imaging modality for clinical assessment of the microcirculation. *Opt Express*, 15:15101–15114, 2007.

[51] T Klyscz, M Jünger, F Jung, and H Zeintl. Cap image : A new kind of computerassisted video image analysis system for dynamic capillary microscopy. *Biomed. Tech.*, 42:168–175, 1997.

[52] A. Bauer, S. Kofler, M. Thiel, S. Elfert, and F. Christ. Monitoring of the sublingual microcirculation in cardiac surgery using orthogonal polarization spectral imaging. *the American Society of Anesthesiologists*, 107(6):939–945, 2007.

[53] S. Schaudig, B. Dadasch, KR. Kellam, and F. Christ. Validation of an analysis software for ops-imaging used in humans. In *Proceedings of the 7th World Congress for Microcirculation*, pages 2–59, 2001.

[54] J Zhong, CL Asker, and EG Salerud. Imaging, image processing and pattern analysis of skin capillary ensembles. *Skin Res Technol*, 6:4557, 2000.

[55] JM Sainthillier, T Gharbi, P Muret, and P Humbert. Skin capillary network recognition and analysis by means of neural algorithms. *Skin Res Technol*, 11:916, 2005.

[56] JGG Dobbe, GJ Streekstra, B Atasever, R van Zijderveld, and C Ince. The measurement of functional microcirculatory density and velocity distributions using automated image analysis. *Med Biol Eng Comput*, 46(7):659–670, 2008.

[57] Qiming Luo and Taghi M. Khoshgoftaar. An empirical study on estimating motions in video stabilization. In *Proc. of the IEEE International Conference on Information Reuse and Integration*, pages 360–366, 2007.

[58] L. Xu and X. Lin. Digital image stabilization based on circular block matching. In *IEEE Trans. Consum. Electron.*, volume 52-2, page 566574, 2006.

[59] Sung-Jea Ko, Sung-Hee Lee, and Kyung-Hoon Lee. Digital image stabilizing algorithms based on bit-plane matching. *IEEE Transactions on Consumer Electronics*, 44:617–622, 1998.

[60] S. Erturk. Digital image stabilization with sub-image phase correlation based global motion estimation. *IEEE transactions on consumer electronics*, 49:1320, 2003.

[61] J. S. Lim. *Two-Dimensional Signal and Image Processing*. Prentice-Hall, 1990.

[62] J. Jin, Z. Zhu, and G. Xu. Digital video sequence stabilization based on 2-d motion estimation and inertial motion filtering. *Real-Time Imaging*, 7:357–365, 2001.

[63] J. Chang, W. Hu, M. Cheng, and B. Chang. Digital image translational and rotational motion stabilization using optical flow technique. *IEEE Transactions on Consumer Electronics*, 48-1:108–115, 2002.

[64] A. Crawford, H. Denman, F. Kelly, F. Pitie, and A. Kokaram. Gradient based dominant motion estimation with integral projections for real time video stabilization. In *International Conference on Image Processing*, volume 5, page 3371 3374, 2004.

[65] C. Erdem and A. Erdem. An illumination invariant algorithm for subpixel accuracy image stabilization and its effect on mpeg-2 video compression. *Elsevier Signal Processing: Image Communication*, 16:837–857, 2001.

[66] Clements L.W., W.C. Chapman, B.M. Dawant, Jr R.L. Galloway, and Miga M.I. Robust surface registration using salient anatomical features for image-guided liver surgery: Algorithm and validation. *Med. Phys.*, 35, 2008.

[67] H. Chui, Win L., R. Schultz, J. Duncan, and A. Rangarajan. A unified non-rigid feature registration method for brain mapping. *Inf. Process. Med. Imaging*, 7, 2001.

[68] M. Söhn, M. Birkner, Y. Chi, J. Wang, D. Yan, B. Berger, and M. Alber. Model-independent, multimodality deformable image registration by local matching of anatomical features and minimization of elastic energy. *Med. Phys.*, 35, 2008.

[69] Jinzhong Yang, Dinggang Shen, Christos Davatzikos, and Ragini Verma. Diffusion tensor image registration using tensor geometry and orientation features. *MICCAI*, 5242, 2008.

[70] J. C. Gee, C. Barillot, L. le Bricquer, D. R. Haynor, and R. Bajcsy. Matching structural images of the human brain using statistical and geometrical image features. *Visualization in biomedical imaging*, 2359, 1994.

[71] J.B.A. Maintz and M.A. Viergever. A survey of medical image registration. *Medical image analysis*, 2, 1998.

[72] B Zitová and J. Flusser. Image registration methods: a survey. *Image and Vision Computing*, 21, 2003.

[73] Jeongho Shin, Sangjin Kim, Sangkyu Kang, Seong-Won Lee, Joonki Paik, Besma Abidi, and Mongi Abidi. Optical flow-based real-time object tracking using non-prior training active feature model. *Real-Time Imaging*, 11(3):204 – 218, 2005.

[74] Yasuyuki Matsushita, Eyal Ofek, Weina Ge, Xiaoou Tang, and Heung-Yeung Shum. Full-frame video stabilization with motion inpainting. *IEEE Transactions on Pattern Analysis and Machine Intelligence*, 28:1150–1163, 2006.

[75] Niall Patton, Tariq M. Aslam, Thomas MacGillivray, Ian J. Deary, Baljean Dhillon, Robert H. Eikelboom, Kanagasingam Yogesan, and Ian J. Constable. Retinal image analysis: Concepts, applications and potential. *Progress in Retinal and Eye Research*, 25:99–127, 2006.

[76] A Hoover, V Kouznetsova, and M Goldbaum. Locating blood vessels in retinal images by piece-wise threhsold probing of a matched filter response. *IEEE transactions on medical imaging*, 19:203–210, 2000.

[77] AK Jain and F Farrokhnia. Unsupervised texture segmentation using gabor filters. *Pattern recognition*, 24:1167–1186, 1991.

[78] M. Franz and R. Schaüffny. Segmentation of blood vessels in subtraction angiographic images. *In Proc. DIC*, pages 215–224, 2003.

[79] Guerrero J, Salcudean SE, McEwen JA, Masri BA, and Nicolaou S. Real-time vessel segmentation and tracking for ultrasound imaging applications. *IEEE TRANSACTIONS ON MEDICAL IMAGING*, 26:1079–90, 2007.

[80] C. Kirbas and F. Quek. A review of vessel extraction techniques and algorithms. *ACM Computing Surveys*, 36:81–121, 2004.

[81] P.J. Haug, R.M. Gardner, K.E. Tate, East TD, Kuperman G, Pryor TA, Huff SM, and Warner HR. Decision support in medicine: examples from the help system. *Comput Biomed Res.*, 27:396–418, 1994.

[82] J. Kaye, U. von Steele, A. Gertner, and M. Niv. Traumaid 2.0, a sketchy guide through uncharted terrain. *Technical Report, University of Pennsylvania*, 1994.

[83] J.R. Clarke, C.Z. Hayward, T.A. Santora, and D.K. Wagner. Computer-generated trauma management plans: comparison with actual care. *World J Surg.*, 26(5):536–538, 2002.

[84] Alireza Osareh and Bita Shadgar. Retinal vessel extraction using gabor filters and support vector machines. *Communications in Computer and Information Science, Advances in Computer Science and Engineering*, pages 356 – 363, 2009.

[85] J. V. B. Soares, J. J. G. Leandro, R. M. Cesar Jr., H. F. Jelinek, and M. J. Cree. Retinal vessel segmentation using the 2-d gabor wavelet and supervised classification. *IEEE TRANSACTIONS ON MEDICAL IMAGING*, 25(9):12141222, 2006.

[86] Alireza Osareh and Bita Shadgar. An automated tracking approach for extraction of retinal vasculature in fundus images. *Journal of Ophthalmic & Vision Research*, 5(1):20, 2010.

[87] Qin Li, Jane You, Lei Zhang, and Prabir Bhattacharya. A multiscale approach to retinal vessel segmentation using gabor filters and scale multiplication. In *IEEE International Conference on Systems*, pages 22–28, 2006.

[88] S Chaudhuri, S Chatterjee, N Katz, M Nelson, and M Goldbaum. Detection of blood vessels in retinal images using two-dimensional matched filters. *IEEE Trans Med Imag*, 8:2639, 1989.

[89] M Sofka and C Stewart. Retinal vessel centerline extraction using multiscale matched filters, confidence and edge measures. *IEEE TRANSACTIONS ON MEDICAL IMAGING*, 25:15311546, 2006.

[90] M Al-Rawi, M Qutaishat, and M Arrar. An improved matched filter for blood vessel detection of digital retinal images. *Computers in Biology and Medicine*, 37:262 267, 2007.

[91] H. Sekiguchi, N. Sugimoto, S. Eiho, T. Hanakawa, and S. Urayama. Blood vessel segmentation for head mra using branch-based region growing. *Syst. Comput Japan*, 36:80–88, 2005.

[92] P. Yim, P. Choyke, and R. Summers. Grayscale skeletonization of small vessels in magnetic resonance angiography. *IEEE Transactions on Medical Imaging*, 19:568576, 2000.

[93] M.E. Martinez-Perez, A.D. Hughes, S.A. Thom, A.A. Bharath, and K.H. Parker. Segmentation of blood vessels from red-free and fluorescein retinal images. *Medical Image Analysis*, 11:47–61, 2007.

[94] J.J. Staal, M.D. Abramoff, M. Niemeijer, M.A. Viergever, and B. van Ginneken. Ridge based vessel segmentation in color images of the retina. *IEEE Transactions on Medical Imaging*, 23:501–509, 2004.

[95] Nancy M. Salem, Sameh A. Salem, and Asoke K. Nandi. Segmentation of retinal blood vessels based on analysis of the hessian matrix and clustering algorithm. In *15th European Signal Processing Conference*, 2007.

[96] Chanjira Sinthanayothin, James F Boyce, Helen L Cook, and Thomas H Williamson. Automated localisation of the optic disc, fovea, and retinal blood vessels from digital colour fundus images. *Br J Ophthalmol*, 83:902910, 1999.

[97] F. Zana and J. C. Klein. Segmentation of vessel-like patterns using mathematical morphology and curvature evaluation. *IEEE Transactions on Image Processing*, 10-7:10101019, 2001.

[98] B. Fang, W. Hsu, and M. Lee. Reconstruction of vascular structures in retinal images. In *International Conference on Image Processing*, volume 2, page 157160, 2003.

[99] SJ Schmugge, WS Kamoun, J Villalobos, MG Clemens, and MC Shin. Segmentation of vasculature for intravital microscopy using bridging vessel snake. In *IEEE International Symposium on Biomedical Imaging: Nano to Macro*, pages 177–180, 2006.

[100] Jinshan Tang and Acton ST. Vessel boundary tracking for intravital microscopy via multiscale gradient vector flow snakes. *IEEE Transactions on Biomedical Engineering*, 51:316–324, 2004.

[101] KW Sum and PYS Cheung. A novel active contour model using local and global statistics for vessel extraction. In *Int. Conf. IEEE Eng. Medicine Biol. Soc. (EMBS)*, page 3126, 2006.

[102] Y. Sun. Automated identification of vessel contours in coronary arteriograms by an adptive tracking algorithm. *IEEE Trans. Med. Imag.*, 8-1:7888, 1989.

[103] X. Gao, A. Bharath, A. Stanton, A. Hughes, N. Chapman, and S. Thom. A method of vessel tracking for vessel diameter measurement on retinal images. In *ICIP01*, page 881884, 2001.

[104] Charles Florin, Nikos Paragios, and Jim Williams. Globally optimal active contours, sequential monte carlo and on-line learning for vessel segmentation. *Computer Vision*, 3953:476–489, 2006.

[105] Xiaoyi Jiang and Mojon D. Adaptive local thresholding by verification-based multithreshold probing with application to vessel detection in retinal images. *IEEE Transactions on Pattern Analysis and Machine Intelligence*, 25:131–137, 2003.

[106] Karel Zuiderveld. Contrast limited adaptive histogram equalization. *Graphics gems IV*, pages 474–485, 1994.

[107] Q.Z. Ye. The signed euclidean distance transform and its applications. In *9th Int. Conference on Pattern Recognition*, pages 495–499, 1988.

[108] R Fabbri, LDF Costa, and JC Torelli. 2d euclidean distance transform algorithms: A comparative survey. *ACM computing surveys*, 40:1, 2008.

[109] A. Meijster, J. Roerdink, and W. Hesselink. A general algorithm for computing distance transforms in linear time. In *Proceedings of the 5th International Conference on Mathematical Morphology and its Applications to Image and Signal Processing*, 2000.

[110] Dempster A.P., Laird N.M., and Rubin D.B. Maximum likelihood from incomplete data via the em algorithm. *Journal of the Royal Statistical Society Series B (Methodological)*, 39 (1):138, 1977.

[111] Bruce D. Lucas and Takeo Kanade. An iterative image registration technique with an application to stereo vision. In *International Joint Conference on Artificial Intelligence*, pages 674–679, 1981.

[112] J.Y. Bouguet. Pyramidal implementation of the lucas kanade feature tracker : description of the algorithm. *OpenCV Document Intel Microprocessor Research Labs*, 2000.

[113] Frank Wilcoxon. Individual comparisons by ranking methods. *Biometrics Bulletin*, 1:80–83, 1945.

VITA

Sümeyra Ümmühan Demir was born in Antalya, Turkey, on January 01, 1982. She is a Turkish citizen. She received a B.Eng degree in Electrical and Electronics Engineering from Dokuz Eylul University in Izmir, Turkey in 2004. She received Master of Science degree from Fatih University in Istanbul, Turkey in 2007. Her research interests include digital signal and image processing, computer-assisted decision making, and pattern recognition.

List of Relevant Publications:

S. Demir, N. Mirshahi, K. Ward, R. Hobson, K. Najarian, '*Vessel Extraction of Microcirculatory Video Recordings Using Multi-Thresholding Based Verification Algorithm*', The Second International Conference on Advances in Biotechnologies (BIOTECHNO 2010), Cancun, Mexico, March 7-13, 2010.

N. Mirshahi, S. Demir, K. Ward, R. Hobson, K. Najarian, '*A Multi-Resolution Entropic-based Image Processing Technique for Diagnostic Analysis of Microcirculation Videos*', The Second International Conference on Advances in Biotechnologies (BIOTECHNO 2010), Cancun, Mexico, March 7-13, 2010.

Sumeyra U Demir, Nazanin Mirshahi, Kevin Ward, Rosalyn S Hobson, Kayvan Najarian, '*Vessel Segmentation Based on Multi-Thresholding for Diagnostic Analysis of Microcirculation*', Circulation. 2009;120:S1491.

Sumeyra Demir, Nazanin Mirshahi, M. Hakam Tiba, Gerard Draucker, Kevin Ward, Rosalyn Hobson and Kayvan Najarian, '*Image Processing and Machine Learning for Diagnostic Analysis of Microcirculation*', IEEE/ICME International Conference on Complex Engineering CME 2009, Phoenix, AZ, USA, April 2009.

Other Publications:

Cihan Ulaş, Sümeyra Demir, Onur Toker, Kemal Fidanboylu, '*Rotation Angle Estimation Algorithms for Textures and Their Real-Time Implementation on the FU-Smart*', ISPA 2007, Istanbul, Turkey, September 2007.

A. Öztekin, A. Nikov, I. Demirci, S. Demir, I.I. Uzonur, '*Usability Evaluation of eLearning Systems by Neural Networks*', 53th Congress of German Human Factors Association GfA2007, Magdeburg, Germany, March 2007.

Work Experience:

Graduate Research Assistant, Department of Electrical and Computer Engineering, Virginia Commonwealth University, Richmond, VA, USA. (August 2007-August 2010)

Research and Teaching Assistant, Electronics Engineering Department, Fatih University, Istanbul, Turkey. (September 2006-June 2007)

Awards:

VCU Graduate School research assistantship